ACCEPTED VERSION

R. Tamblyn, D.Brown, M.Hand, L.Morrissey, C.Clark, R. Anczkiewicz

The 2 Ga eclogites of Central Tanzania: directly linking age and metamorphism

Lithos, 2020; 380-381:105890-1-105890-13

Final publication at: http://dx.doi.org/10.1016/j.lithos.2020.105890

The 2 Ga eclogites of central Tanzania: directly linking age and metamorphism

R. Tamblyn[1*], D. Brown[1], M. Hand[1], L. Morrissey[2,1], C. Clark[3] and R. Anczkiewicz[4]

[1] Department of Earth Sciences, The University of Adelaide, Adelaide, Australia

[2] Future Industries Institute, The University of South Australia, Adelaide, Australia

[3] School of Earth and Planetary Sciences, Curtin University, Perth, Australia

[4] Polish Academy of Sciences, Kraków, Poland

* Corresponding author: renee.tamblyn@adelaide.edu.au

Abstract

The ca. 2 Ga retrogressed eclogites in the Usagaran Belt in central Tanzania are among the oldest documented eclogites in the world. As such, they have been used to pinpoint the thermal conditions of the onset of modern style subduction on Earth. Two samples of retrogressed mafic eclogite have been interrogated to reconstruct the metamorphic history of the subducted crust. The samples are several kilometres apart, separated by a mylonitic upper amphibolite-transitional granulite foliation. Lu–Hf garnet geochronology pinpoints eclogite metamorphism at 1994 ± 9 Ma, supported by rutile U–Pb geochronology. Zircon U–Pb geochronology supports subduction metamorphism at ca. 2000 Ma. Mineral equilibria modelling and Zr in rutile thermometry suggests the retrogressed eclogites reached a minimum pressure of 18 kbar at approximately 800 °C, consistent with a warm subduction thermal gradient. These conditions were followed by amphibolite-granulite-facies overprinting. Proposed tectonic models for the formation of the eclogites involve either east-dipping subduction of the Tanzanian Craton margin, or west-dipping subduction of oceanic crust under the Tanzanian Craton. The retrogressed eclogites were likely exhumed via slab breakoff driven buoyancy of the oceanic crust and transferred to shallow crustal levels in a back arc position. This data, combined with data from eclogites from the Eburnian-Transamazonian and Ubende orogens, demonstrate the possible existence of a large subduction system on the margin of west Africa from ca. 2.1–1.9 Ga. This system has led to the preservation of several eclogitic rocks, which suggests that modern style subduction was operating on significant geographic and temporal scales at this time.

Keywords: eclogite, high-pressure metamorphism, subduction, Usagaran Belt, secular evolution; Palaeoproterozoic eclogite

Highlights:

- Eclogite-facies metamorphism in the Usagaran Belt occurred at ca. 1994 Ma as dated by garnet Lu–Hf.
- Peak conditions were at least 18 kbar at approximately 800 °C, pointing to warm subduction thermal gradients in the Palaeoproterozoic.
- Possible tectonic scenarios for formation of the Usagaran eclogites involve east- or west-dipping subduction followed by buoyancy driven exhumation and emplacement into a back arc basin.

1. Introduction

The appearance of eclogite-facies mineral assemblages in the geological record has long been used to pinpoint the emergence of subduction on Earth. While abundant in the Neoproterozoic and Palaeozoic, subduction related eclogite-facies rocks are scarce throughout the Archaean to Mesoproterozoic. The oldest subduction related eclogite-facies rocks appear in the geological record in the Palaeoproterozoic suggesting the emergence of 'modern style' subduction at around 2 Ga (Brown & Johnson, 2018; Palin et al., 2020). This raises debate as to why subduction related rocks appear at this time. One argument is that thermal gradients on Earth were too warm to produce eclogite-facies rocks prior to the Palaeoproterozoic. Conversely, eclogite-facies rocks may have been produced before and during the Palaeoproterozoic, but not preserved in the geological record. Regardless, constraining the *P–T–t* evolutions of ancient eclogites enables the timing of subduction related metamorphism, the thermal state of the subduction system and possible exhumation mechanisms to be understood, permitting insight to ancient tectonic processes.

Palaeoproterozoic-aged eclogite-facies rocks have been described in few localities and are often retrogressed to amphibolite or granulite conditions. Some of the oldest subduction related eclogite-facies rocks are preserved in the Eburnian-Transamazonian Orogen in southern Cameroon (ca. 2090 Ma; Loose & Schenk, 2018), the Congo Craton in the Democratic Republic of Congo (ca. 2090 Ma; François et al., 2018), the Usagaran Orogen in Tanzania (ca. 1991 Ma; Möller et al., 1995; Collins et al., 2004), the Snowbird Tectonic Zone in Canada (ca. 1904 Ma; Baldwin et al., 2004), the Belomorian Province in Russia (ca. 1940–1890 Ma; Herwartz et al., 2012; Xu et al., 2018; Yu et al., 2019), the Ubendian Orogen in Tanzania (ca. 1886 Ma; Boniface et al., 2012) and in the Trans-Hudson Orogen in North America (ca. 1831 Ma; Weller & St-Onge, 2017). A significant volume of work has been dedicated to investigating these high-pressure rocks, however, only some have been studied with modern, integrated petrologic and geochronologic techniques (i.e. petrochronology).

The *P*–*T* conditions for Usagaran eclogite-facies metamorphism have been constrained from mineral equilibria models (Brown et al., 2020) and the eclogite-facies rocks in the Usagaran Belt have been dated using zircon at 1986 ± 29 Ma (Collins et al., 2004). However, the absence of data on the trace-element compositions of the zircons means this age cannot be directly linked to the formation of the eclogite-facies mineral assemblages. No study has integrated modern geochronology and mineral equilibria modelling. This study presents garnet Lu–Hf and zircon, rutile and titanite U–Pb geochronology tied to trace-element chemistry, trace-element thermometry and mineral equilibria modelling to constrain the precise timing and *P*–*T* conditions of eclogite-facies metamorphism in the Usagaran Belt.

2. Geological background

The Usagaran Belt in central Tanzania contains relic eclogite-facies mineral assemblages. Eclogite-facies metamorphism is interpreted to have occured during subduction of the rifted margin of the Tanzanian Craton (Möller et al., 1995; Reddy et al., 2003; Collins et al., 2004). The Usagaran Belt is bordered to the north and west by the ca. 2700 Ma Tanzanian Craton, to the east by the ca. 640–610

Ma East-African Orogen, and to the south-west by the Ubendian Belt (Fig. 1a). The Ubendian Belt is interpreted to have experienced high-pressure metamorphism between ca. 1870–1865 Ma (Boniface et al., 2012), leading to the formation of now sparsely preserved eclogite.

The Usagaran Belt is divided into two lithotectonic units, the Konse Group and the Isimani Suite (Fig. 1b). The Konse Group formed at ca. 1895 Ma, and unconformably overlies the Isimani Suite and the Tanzanian Craton (Mruma, 1989; Reddy et al., 2003). It is comprised of volcanic and sedimentary successions metamorphosed to greenschist facies (Mruma, 1989). It also contains pillow basalts which have a T- to N-MORB composition (Boniface & Tsujimori, 2018). The Isimani Suite has been described in detail by Mruma (1989) and Brown et al. (2020). It is dominated by mafic and metapelitic amphibolite-facies gneisses, some of which are migmatitic. It also contains rare whiteschist assemblages (Mori et al., 2018). Coarse-grained metapelitic gneisses (~ 5 m thick) are interlayered with amphibolite-granulite-facies mafic rocks (~10–50 m thick), which are boudinaged. Comparatively low strain domains of these mafic rocks contain the mineral assemblage garnet + clinopyroxene + hornblende + plagioclase + quartz ± orthopyroxene. Omphacite included in garnet was found by Möller et al. (1995) in one of these domains, confirming a precursor eclogite-facies mineral assemblage.

SHRIMP U–Pb geochronology from zircons from the retrogressed eclogite assemblage returned an age of 1986 ± 29 Ma (Collins et al., 2004). However, in absence of trace-element compositions of the zircons, it is not clear if these zircons grew during eclogite-facies metamorphism. The metapelitic gneisses and migmatitic rocks returned similar ages, with SHRIMP U–Pb zircon ages of ca 1997–1989 Ma (Mruma, 1989; Collins et al., 2004). Monazites from metapelitic rocks give $^{207}Pb/^{206}Pb$ ages of 1999 ± 2 Ma and 2000 ± 2 Ma (Möller et al., 1995), however the relationship between the monazite and the bulk silicate mineral assemblages in the metapelites is not clear. Collins et al. (2004) inferred that these U–Pb ages in the Isimani Suite reflected eclogite-facies metamorphism of the entire unit, despite the vast bulk of the Isimani Suite not consisting of eclogite-facies rocks. This was confirmed by Brown et al. (2020), who proposed the mafic and metapelitic gneisses from Yalumba Hill and Ruaha River were coevally buried to high-pressure conditions. The relict eclogite assemblage had previously been interpreted to have formed at *P–T* conditions of ~ 18 kbar and 750 °C (Möller et al., 1995), or at least 15 kbar and 750–850 °C (Herms, 2002). These estimates were based in part on using the composition of demonstrably retrograde plagioclase and derived from a combination of texturally peak and retrograde minerals. Brown et al. (2020) calculated conditions of at least 18 kbar and 750 °C for relic eclogite, with the retrograde evolution passing through conditions of ~8 kbar and ~700 °C. The metapelitic garnet-kyanite-bearing gneisses formed at *P–T* conditions of at least ~17 kbar and 700 °C (Brown et al., 2020). Talc and kyanite bearing amphibolites 5 km south of Yalumba Hill in the Isimani Suite reached peak pressures of at least 10 kbar at 600–750 °C (Mori et al., 2018). After high-pressure metamorphism, the Isimani Suite is interpreted to have undergone a pressure decrease to amphibolite/granulite conditions, at conditions of 6–8 kbar and 520–600 °C as recorded by metapelitic assemblages (Brown et al., 2020).

The timing of retrograde metamorphism is constrained by a U–Pb titanite age of 1996 ± 2 Ma from amphibolite-facies mafic gneiss (Möller et al., 1995). This is supported by a SHRIMP U–Pb zircon age of 1992 ± 2 Ma from a pegmatite dyke that cross-cuts amphibolite-facies fabrics that overprint the eclogite assemblages (Collins et al., 2004). The unconformably overlying Konse Group contains post-tectonic granite with a SHRIMP U–Pb zircon age of 1877 ± 7 Ma (Reddy et al., 2003), suggesting that Isimani Suite metamorphism and deformation had concluded by this time. Furthermore, the Usagaran belt contains numerous I-type syn- to post-tectonic granitoids interpreted to be arc magmas, which intruded between ca. 1940–1877 Ma (Sommer et al., 2005a). The calc-alkaline volcanics of the Ndembera group also formed at this time (ca. 1920–1870 Ma; Sommer et al., 2005a; Bahame et al., 2016).

An early Palaeozoic greenschist facies overprint has been identified in the Usagaran Belt, attributed to the development of the East African Orogen (Möller et al., 1995; Reddy et al., 2003;

Collins et al., 2004; Fritz et al., 2013). Discordant rutile U–Pb data from metapelitic rocks of the Isimani Suite has a lower intercept age of 501 ± 26 Ma (Möller et al., 1995). Muscovite from an Isimani Suite orthogneiss gave an $^{40}Ar/^{39}Ar$ plateau age of 535 ± 2 Ma (Reddy et al., 2003).

The interpreted tectonic evolution of the Usagaran Belt involves the subduction of the margin of the Tanzanian Craton (Reddy et al., 2003). Brown et al. (2020) suggested this convergence involved crustal thickening and shallow subduction of mafic lithologies and enclosing pelites. Following burial, slab breakoff induced buoyancy-driven exhumation, where the formation of an extensional system allowed the rock package to be exhumed within rapid timeframes (up to 20 Myr; Brown et al., 2020). It is clear the subducted margin comprised pelitic and mafic lithologies, now preserved as the kyanite-garnet gneisses and retrogressed eclogites of the Isimani Suite (Brown et al., 2020). Geochemistry suggests the mafic eclogite was derived from a MORB-type source, although Sm–Nd and Hf isotopes suggest both the mafic and pelitic rocks of the Isimani Suite are evolved (Möller et al., 1998; Maboko, 2000; Brick, 2011). Furthermore, the pelitic rocks appear to be derived from the Tanzanian Craton, and an unidentified ca. 2600–2460 Ma source (Collins et al., 2004).

3. Samples

Two mafic samples from Yalumba Hill (Fig. 1b) were selected for this study based on their mineral assemblages and suitability for geochronology. Sample T01-40 is the same sample as that studied by Collins et al. (2004). T01-40 is granoblastic and is partially retrogressed to amphibolite-facies and T06-09 has a weak foliation and is partially retrogressed to granulite-facies. The two samples are several kilometres apart (Fig. 1b), and are separated by mylonitic shear fabrics. Taken together, both samples allow for investigation of the full *P–T–t* evolution of the mafic lithology at Yalumba Hill.

3.1 T01-40

T01-40 is granoblastic, and contains garnet, clinopyroxene, hornblende, plagioclase, quartz, rutile, ilmenite, magnetite, titanite, epidote, apatite and zircon. Garnet is euhedral-subhedral, up to 1500 μm in size and contains fine-grained inclusions of quartz, plagioclase, hornblende, rutile and titanite, and rare clinopyroxene, epidote, ilmenite, apatite and zircon (Fig. 2a,e,f). It is separated from the matrix by coronae of plagioclase, or by symplectic intergrowths of plagioclase and hornblende, or plagioclase, magnetite and ilmenite (Fig. 2a,b). Clinopyroxene forms coarse symplectites up to 1500 μm, where plagioclase forms elongate grains along clinopyroxene cleavage planes (Fig. 2d). Fine-grained magnetite also occurs in these symplectitic textures. Clinopyroxene is also replaced and rimmed by hornblende, which forms subhedral grains up to 200 μm (Fig. 2b,d). Quartz forms as euhedral grains throughout the matrix (up to 500 μm; Fig. 2a,b). Rutile grains occur only as inclusions in garnet, and often contain ilmenite exsolution lamellae (Fig. 2e). Ilmenite and magnetite are occasionally intergrown and form irregular grains throughout the matrix, which are up to 500 μm in size (Fig. 2c). Rare apatite and zircon grains (~ 50 μm) are present in the matrix. T01-40 contains a small 5 mm wide quartz vein, mantled by symplectitic clinopyroxene and garnet.

3.2 T06-09

T06-09 is weakly foliated, and generally finer grained than T01-40. It contains garnet, clinopyroxene, hornblende, plagioclase, orthopyroxene, quartz, rutile, ilmenite, magnetite, apatite and zircon. Garnet forms irregular grains (up to 1500 um, but generally smaller) which contain abundant fine-grained inclusions of quartz, plagioclase and rutile, and rarer clinopyroxene, hornblende, zircon and chalcopyrite (Fig. 2g,k,l). Clinopyroxene in the matrix is sieve textured with plagioclase and magnetite inclusions (Fig. 2h), or extensively broken down to form fine-grained masses with plagioclase, hornblende and rare orthopyroxene (Fig. 2h,i). In some instances, these minerals form composite grains, and the original size of the clinopyroxene is up to 1000 μm. Garnet and clinopyroxene are separated by coronae of plagioclase with symplectic fine grained magnetite, or sometimes double coronae of plagioclase and hornblende, with hornblende on the clinopyroxene margin (Fig. 2g,i). Quartz forms euhedral grains up to 500 μm in size throughout the matrix (Fig. 2h).

Ilmenite and magnetite form irregular grains up to 1000 µm long throughout the matrix (Fig. 2g). Rare apatite and zircon occur throughout the matrix. A thin hornblende vein 2 mm wide cross cuts the sample, encompassing and replacing clinopyroxene grains (Fig. 2j).

3.3 A previous eclogitic assemblage

Previous authors have argued for an eclogitic assemblage in the mafic rocks of Yalumba Hill (Möller et al., 1995; Herms, 2002; Collins et al., 2004; Brown et al., 2020). Originally, this argument was based on the existence of rare omphacite inclusions in garnet (Möller et al, 1995), but has since been supplemented with petrologic arguments and mineral equilibria modelling from Brown et al. (2020). No omphacite inclusions in garnet could be detected in this study, perhaps owing to the rarity of clinopyroxene inclusions in general. The existence of symplectitic intergrowths of Na-poor clinopyroxene and plagioclase has been used to argue for a previous Na-bearing clinopyroxene, namely omphacite, which has ejected its Na component to form albitic plagioclase during retrograde conversion to Na-poor clinopyroxene (e.g. Loose & Schenk, 2018). The abundance of well-developed symplectitic textures in both T01-40 and T06-09 would suggest that the previous clinopyroxene was Na-rich (Fig. 2). Reintegration of albitic plagioclase into the clinopyroxene shows that the precursor clinopyroxene was ferro-omphacite in composition (Brown et al., 2020). Additionally, the present garnet mode for each sample is ~ 25%, and prior to the development of retrograde plagioclase coronae, would have been up to ~ 40%. As such, samples T01-40 and T06-09 are referred to as retrogressed eclogites.

4. Methods

4.1 Q450 Scanning Electron Microscopy

Samples were imaged using a FEI Quanta 450 scanning electron microscope (SEM) with an attached Oxford Ultim Max Large Area energy dispersive X-Ray spectrometer (EDS) detector at

Adelaide Microscopy, Australia. Images were acquired in back scattered electron (BSE) mode with an accelerating voltage of 20 kV and a spot size of 4, at a working distance of 10 mm. Minerals were identified from EDS spectra and semi-quantitative compositional data, which were processed using Oxford Aztec EDS software.

4.2 Electron Probe Micro Analyses and X-Ray mapping

Mineral chemistries and garnet maps were obtained using a Cameca SX-5 WDS electron microprobe. Spot analyses used a beam current of 20 nA and an accelerating voltage of 15 kV, with an andradite crustal used for calibration. Element maps used a 200 nA beam current and an accelerating voltage of 15 kV. Ca, Fe, Mn and Mg were mapped using Wavelength Dispersive Spectrometers (WDS).

4.3 LA–ICP–MS garnet spot analyses and mapping

Major (Si, Al, Ca, Fe, Mg and Mn), trace (Ti, Cr, V, Y and Hf) and rare earth elements (La, Ce, Pr, Nd, Sm, Eu, Gd, Tb, Dy, Ho, Er, Tm, Yb and Lu) were analysed by single spots and mapping of garnet using an ASI m50 LA–ICP–MS with an Agilent 7900 MS at Adelaide Microscopy, Australia. The spot size was 30 µm, with a repetition rate of 5 Hz and a laser energy at the sample surface of 3.2 Jcm^{-2}. The primary reference material used for corrections was NIST612. The individual data spots and maps were processed in Iolite (Paton et al., 2011) using Ca as the internal reference element, as measured in the garnets by EPMA (Table A. 2). Rare earth element (REE) plots were made using GCDkit (Janoušek et al., 2006).

4.4 Garnet Lu–Hf geochronology

Garnet was separated using conventional crushing, magnetic separation, and hand-picking to obtain pure mineral samples. Whole rock samples were obtained by hand-pulverising presentative parts of the rock in an agate mortar. Lu–Hf analyses were collected at the Kraków Research Centre, Institute of Geological Sciences, Polish Academy of Sciences. Methods followed Anczkiewicz & Thirlwall (2003) with modifications for the Lu–Hf method from Anczkiewicz et al. (2004). JMC475 measured over the course of the analyses yielded $^{176}Hf/^{177}Hf$ = 0.282158 ± 8 (n = 7; 2σ). Isochron ages were calculated using IsoplotR (Vermeesch, 2018), all certainties are reported as 2σ.

4.5 *Zircon U–Pb geochronology and trace-elements*

Zircon grains were liberated from the samples using a SELFRAG electric pulse disaggregation system at Curtin University, and were separated using magnetic separation, heavy liquid and picking techniques. The grains were mounted in epoxy resin, polished to expose their cross section, and then imaged in BSE and CL. This was done using a Quanta600 Scanning Electron Microscope (SEM) at Adelaide Microscopy. U–Pb and trace-element compositional data were collected using the laser ablation split stream (LASS) system at the GeoHistory Facility in the John de Laeter Centre at Curtin University. Zircons were ablated using a Resonetics RESOlution M–50A–LR system, U–Pb isotopes were measured using a Nu Plasma II multi-collector inductivity coupled plasma mass spectrometer and trace-elements were measured using an Agilent 8900s quadrapole inductivity coupled plasma mass spectrometer. Samples were ablated using a spot size of 24 µm and a 5 Hz repetition rate, and a laser energy at the sample surface of 2.1 Jcm^{-2}. The acquisition time for each analysis was 115 s, including 40 s of background, 35 s of ablation, and a further 40 s of background. Time resolved mass spectra were reduced using Iolite (Paton et al., 2011) and in-house Microsoft Excel macros. Zircon standard GJ1 (Jackson et al., 2004) was used as a primary reference material. Zircon standards Pleśovice (337.13 ± 0.37 Ma; Sláma et al., 2008), 91500 (1065.3 ± 0.3 Ma; Wiedenbeck et al., 1995) and OGC (3465 ± 0.6 Ma; Stern et al., 2009) were used as secondary reference material. Over the course of the analyses all secondary reference materials yielded concordant U–Pb ages, Pleśovice yielded a weighted mean $^{206}Pb/^{238}Pb$ age of 339 ± 2 Ma (n = 11, MSWD = 1.8), 91500 yielded a weighted mean $^{207}Pb/^{206}Pb$ age of 1067 ± 2 Ma (n = 18, MSWD = 1.08), and OGC yielded a weighted mean $^{207}Pb/^{206}Pb$ age of 3460 ± 4 Ma (n = 19, MSWD = 1.3). Trace-element data were reduced using GJ1 as the primary standard (Zr = 3.55 ppm; Liu et al., 2010) and using ^{29}Si as the internal standard element (15.2 wt%). NIST glasses SRM610 and SRM612 were monitored to verify the accuracy of the trace-element data reduction, they returned Zr contents of 452 ppm (expected = 452 ppm) and 42 ppm (expected = 44 ppm) respectively. REE plots were made using GCDkit (Janoušek et al., 2006).

4.6 Rutile U–Pb geochronology and trace-elements

Rutile grains were liberated from the samples using a SELFRAG electric pulse disaggregation system at Curtin University, and were separated using magnetitic separation, heavy liquid and picking techniques. The grains were mounted in epoxy resin and polished through to expose their cross section, and imaged using a Quanta600 Scanning Electron Microscope (SEM) to identify the presence of inclusions and/or exsolution. The rutile grains were analysed for U–Pb isotopes and trace element concentrations simultaneously using an ASI m50 LA–ICP–MS with an attached 7700 MS at Adelaide Microscopy, Australia. Grains were ablated using a spot size of 51 µm, a frequency of 5 Hz, and an intensity of 5 Jcm^{-2}. The acquisition time for each analysis was 80 s, including 30 s of background measurement of 50 s of ablation. The primary reference standard R10 was used to correct for U–Pb elemental fractionation, mass bias and instrument drift over the course of the analyses (Luvizotto et al., 2009), and the R19 standard was used as a secondary reference (493 ± 10 Ma; Luvizotto et al., 2009; Zack et al., 2011). The synthetic glass standard NIST610 was used to correct for Zr and trace-element concentrations. Ti was used as the internal reference element for the trace-element analyses (unknowns were corrected to 59.94 wt % Ti). Corrections were done using the software Iolite (Paton et al., 2011) and age calculations were done using IsoplotR (Vermeesch, 2018). R19 was concordant and returned a weighted mean $^{206}Pb/^{238}U$ age of 496 ± 5.31 Ma (MSWD = 0.85, n = 20) over the course of the analyses. Temperature estimates were calculated from Zr concentrations (in ppm) using the pressure dependent calibration of Tomkins et al. (2007).

4.7 Mineral equilibria modelling

Mineral equilibria forward models were calculated using the code THERMOCALC (v. 345i), with the internally consistent thermodynamic dataset ds62 (Holland and Powell, 2011). The activity-composition (*a*–*x*) models of Green et al. (2016) were used, in the model chemical system MnNCFMASHTO. Potassium was omitted from the model chemical system as the amount measured by whole rock chemistry was negligible (< 0.3 wt%; Table. A. 1).

Whole rock geochemistry for the samples was acquired using X-ray fluorescence spectrometry at Franklin & Marshall College, Pennsylvania (Table A. 1). The whole-rock compositions were adjusted for the presence of apatite, which is present in the samples in minor proportions and contains CaO, but cannot be modelled in the current chemical system. To assess the sensitivity of the mineral equilibria models to the oxidation state of each sample, pressure-molar oxygen (*P*–*M*o) models were calculated prior to *P*–*T* modelling (Fig. B. 1). The constraints were compared with Fe_2O_3 values calculated from electron microprobe analyses of Fe^{3+} bearing minerals and their modal proportions (Table A. 2; Droop, 1987). H_2O content in each sample was obtained by using the average composition of amphibole (the only hydrous metamorphic mineral in each rock) derived from electron microprobe analyses and its modal proportion in each sample (Table A. 2). This was done as loss on ignition (LOI) values obtained from the whole rock geochemistry are likely to have been affected by minor low-temperature alteration.

Modal proportions of each mineral were determined by acquiring Mineral Liberation Analysis (MLA) images of each thin section. This was done using a FEI Quanta600 SEM at Adelaide Microscopy, Australia. Pixel counting using image analysis software was conducted on the resultant images and proportions were converted from volume % to atom-based mol % for direct comparison with THERMOCALC outputs (Table 1; Holland and Powell, 2011). Modelled mineral modal proportions and compositions were calculated using the software TCInvestigator (Pearce et al., 2015).

Table 1: *Modal proportions of minerals in samples in 1-atom-normalised %, to comply with modes calculated in THERMOCALC.*

	T01-40	**T06-09**
Hornblende	0.09	0.06
Garnet	0.23	0.23
Clinopyroxene	0.32	0.34
Quartz	0.04	0.06
Plagioclase	0.28	0.28
Magnetite	0.02	0.01
Ilmenite	0.02	0.02
Rutile	< 0.01	< 0.01
Epidote	< 0.01	-
Titanite	< 0.01	-
Orthopyroxene	-	0.01

5. Results

5.1 Electron microprobe analysis and mapping

Mineral compositions, end member proportions and THERMOCALC compositional variables are provided in Table A. 2 and garnet maps and traverses are in Figure 3. Additional garnet maps are provided in Figure B. 2. Garnet grains from T01-40 are dominantly almandine and show preservation of prograde zoning. Almandine contents decreases from 0.57 in the core to 0.52 in the rim. Spessartine also decreases from 0.06 in the core to 0.02 at the rims (Fig. 3a,c), whereas grossular and pyrope contents increase from 0.24 and 0.07 in the core to 0.25 and 0.1 in the rims, respectively. The very outer ~ 50 µm of the garnet shows a slight increase in spessartine content (Fig. 3a), accompanied by a slight increase in almandine and a slight decrease in pyrope. In contrast, garnet from T06-09 shows flat spessartine profiles despite being essentially the same size as the garnets in T01-40. The garnet cores in T06-09 contain X_{sps} of ~0.1 spessartine, increasing to 0.2 at the outermost ~ 50 µm of the garnet (Fig. 3b). The garnets are also dominantly almandine, the core is 0.46 almandine which increases to 0.54 towards the rim, corresponding to a core pyrope concentration of 0.14 which decreases slightly to 0.13 towards the rim (Fig. 3b,d). Grossular content is patchy throughout the grain, ranging from 0.24 to 0.26.

Clinopyroxene that occurs in symplectites with plagioclase in both samples is dominantly diopsodic. Matrix clinopyroxene in T01-40 contains 72.8% diopside, 19.6% hedenbergite, 4.5% jadeite and 3.3% aegirine, with a X_J value of 0.08 and an X_{Fe} of 0.21 (X_J = Na/Na+Ca on the M4 site, X_{Fe} = Fe/Fe+Mg). Clinopyroxene included in the cores of garnet contains 63.2% diopside, 25.7% hedenbergite, 10% jadeite and 1% aegirine, with a slightly higher X_J value of 0.11 and an X_{Fe} value of 0.29. Clinopyroxene in T06-09 contains 80.3% diopside, 13.8% hedenbergite, 4.3% jadeite and 1.7% aegirine. It has a X_J of 0.0596 and an X_{Fe} of 0.15.

Amphibole in T01-40 and T06-09 is pargasite (following classification of Locock, 2014). In T01-40 amphibole has a X_{Fe} of 0.3, and a X_{Ti} of 0.07 (X_{Fe} = Fe/Fe+Mg, X_{Ti} = proportion of Ti on the M2 site as defined by the THERMOCALC *a–x* file). In T06-09 amphibole has a X_{Fe} of 0.33 and a X_{Ti} of 0.08.

Plagioclase is dominantly albitic in composition, and is zoned when forming coronae around garnet grains, as can be seen in the Ca EPMA X-ray maps (Fig. 3). Plagioclase coronae that mantles garnet in T01-40 contain 81% albite and 19% anorthite, and plagioclase that mantles matrix minerals contain 73% albite and 27% anorthite. Plagioclase inclusions in the cores of garnets in T01-40 contain 74–75% albite and ~ 25% anorthite. In T06-09, cores of well-developed plagioclase coronae that mantles garnet contain 74% albite and 26% anorthite, and rims which mantle matrix minerals contain 66% albite and 34.1% anorthite. In all plagioclase, sanadine components are low (0.2–0.4%).

Orthopyroxene occurs in T06-09 and is 54–55% enstatite and 38–41% forsterite, the X_{Fe} (Fe/Fe+Mg) ranges from 0.39–0.42. Ilmenite in the samples has minor proportions of hematite (6–11%) but is dominantly ilmenite (89–94%). Magnetite in T06-09 and T01-40 is 99% magnetite and less than 1% other end members. Titanite in T01-40 contains up to 1.43 wt% Al_2O_3, 0.53 wt% FeO and 0.39 wt % F.

5.3 Garnet REE LA-ICP-MS maps

Garnets were mapped for trace and rare earth elements to assist with interpretation of Lu–Hf geochronology and mineral reactions during prograde growth. Garnets of comparable sizes were mapped in-situ from each sample. Quantitative spot analyses are in Table A. 3. Semi-quantitative maps are in Figure 4 and Mn is shown for comparison. Additional maps are in Figure. B. 2. Garnets from T01-40 and T09-06 preserve distinctly different internal trace-element compositional patterns. Garnets from T01-40 (Fig. 4a-j) preserve Y (up to ~ 400 ppm) and Lu (up to ~ 6 ppm) enrichments in their cores, consistent with Rayleigh fractionation during prograde growth (e.g. Otamendi et al., 2002). These enriched cores can also be seen in much smaller garnets mapped in the images, which are only ~ 100 μm in diameter (e.g. Fig. 4b,c). They also contain a diffuse Y and Lu enriched ring (up to ~ 150 and 2 ppm in Y and Lu respectively; most evident in Fig. 4g-h), and a very narrow outer rim enrichment of Y and Lu, typical of garnets that have been partially resorbed (e.g. Carlson et al., 2012). Cr and V concentrations in the garnets from T01-40 are up to ~ 200 ppm, and show intriguing distributions. Cr is distributed as elongate enrichments throughout the garnet grains (indicated by white dashed lines; Fig. 4d,i), with a discontinuous Cr enrichment in the outermost rim (Fig. 4d,i). V shows a subtle enrichment in the garnet cores, and remains in low concentrations throughout the garnet grain until a slight enrichment in the outermost rim that is coincident with the discontinuous Cr enrichment (Fig. 4e,j). Additionally, there are small granular Cr and V enriched areas in the garnet indicated by white arrows, that occasionally correspond to discrete depletions in Y and Lu (Fig. 4). Quantitative spot analyses of garnets normalised to chondrite are in Figure 5. Garnet in T01-40 shows strong core-rim zoning, with cores enriched in Lu and the HREEs but comparatively depleted in Sm–Tb, and rims comparatively depleted in Lu and HREEs but showing a slight enrichment in Sm–Tb (Fig. 5a).

Compositional patterns in garnets from T06-09 (Fig. 4k-t) are more difficult to interpret, as it is unclear whether they are continuous large porphyroblasts or amalgamations of smaller garnet grains. Larger garnets (Fig. 4l,m) show Y and Lu depletions in their cores, with rimward enrichment of up to approximately 100 ppm Y and 2 ppm Lu. There is a narrow outer rim enriched in Y and Lu, consistent with partial resorption. Smaller garnets show flat Y and Lu (~ 10 and < 0.5 ppm respectively) profiles with very narrow outer enriched rims. Cr concentrations in garnets from T06-09 are low (close to detection limit), but show a diffuse and irregular enrichment towards the rims (Fig. 4n,s). V however shows an enrichment in the core of large garnets (up to 200 ppm; Fig. 4o), which does not correspond to the Y and Lu depleted core. Unlike the large garnet, the smaller garnet shows slight V enrichments close to its rims which correspond to Cr enrichments (Fig. 4t). In spot transects, garnets in T06-09 show a flat REE profile which is unchanging from core to rim (Fig. 5b).

5.3 Garnet Lu–Hf geochronology

Garnet and whole rock Lu–Hf concentrations and ratios can be found in Table A. 4, and isochrons in Figure 6. Reported uncertainties are 2σ. The whole rock and garnet 1, 2, and 3 aliquots from T01-40 give an isochron age of 1994 ± 9 Ma (Fig. 6a; MSWD = 0.98; initial $^{176}Hf/^{177}Hf$ = 0.283227 ± 0.000010). Garnet aliquot 4 was omitted due to an anomalously low $^{176}Lu/^{177}Hf$ ratio. In sample T06-09, garnet aliquot 4 was also omitted from the age calculations, due to an anomalously high $^{176}Lu/^{177}Hf$ ratio. The remaining three garnet aliquots in T06-09 have lower $^{176}Lu/^{177}Hf$ ratios than T01-40, and do not lie on an isochron with the whole rock analysis. When combined with the whole rock analysis, they give an age of 2138 ± 43 Ma (Fig. 6b; MSWD = 17; initial $^{176}Hf/^{177}Hf$ = 0.2787±0.0019). If the whole rock fraction is omitted the remaining three garnet aliquots give an isochron age of 1959 ± 31 Ma (Fig. 6c; MSWD = 0.018; initial $^{176}Hf/^{177}Hf$ = 0.28203 ± 0.0067).

5.4 Zircon U–Pb geochronology and trace-elements

Isotopic and trace-element data for zircon can be found in Table A. 5. Data for T01-40 and T09-09 are presented in Figure 7. Analyses with 100(1-α)% confidence ellipses that intersect concordia are defined as concordant and have been used in the age calculations, the errors on the ellipses are 2se.

In sample T01-40, zircons are rounded to sub-rounded and range from ~ 50–120 μm in their longest dimension (Fig. 7a). The CL responses often show irregular and patchy zoning and less common sector zoning (Fig. 7a). There is variation in CL response between grains, however no systematic core-rim relationships were observed. Seven analyses were excluded from age calculations as they were not concordant. The remaining seventy-seven analyses from T01-40 do not produce a concordia age. There is some dispersion in the age data, as can be seen in the $^{207}Pb/^{206}Pb$ age weighted mean plot (Fig. 7c). The individual spot ages produce a weighted mean $^{207}Pb/^{206}Pb$ age of 2023.7 ± 9.4 Ma (MSWD = 1.84; *n* = 77; all reported uncertainties on ages reflect the approximate 100(1-α)% confidence interval with overdispersion). By comparison, concordant analyses produce a weighted mean $^{207}Pb/^{235}U$ age of 2007 ± 5.3 Ma. (MSWD = 0.92) and a weighted mean $^{206}Pb/^{238}U$ age of 1993.4 ± 8.4 Ma (MSWD = 0.90). Individual spot age variation is not correlated to trace-element composition, Th/U ratio or CL response (Fig. 7c).

Zircons from T06-09 are rounded to sub-rounded and ~ 50–200 μm in diameter. The zircons display variation in CL response between grains and complex internal structures (Fig. 7b). They commonly show irregular and discontinuous zoning, as well as rarer fir-tree zoning and sector zoning typical of metamorphic zircons in mafic rocks (Corfu et al., 2003). The grains commonly show a thin (~ 5 μm) rim that has a dark CL response. However, these rims were too thin to be targeted for geochronology. The data show a possible lead loss trend. Fourteen analyses were excluded from age calculations as they were not concordant. The remaining thirteen analyses from T06-09 produce a concordia age of 2010.1 ± 7.3 Ma (MSWD = 1.7; Fig. 7b), a weighted mean $^{207}Pb/^{206}Pb$ age of 2010.6 ± 10.3 Ma (MSWD = 2.02; Fig. 7d), a weighted mean $^{207}Pb/^{235}U$ age of 2009.7 ± 6.9 Ma (MSWD = 2.32) and a weighted mean $^{206}Pb/^{238}U$ age of 2008 ± 7.9. Ma (MSWD = 1.52). Similar to T01-40, individual spot ages are not correlated to trace-element composition, Th/U ratio or CL response (Fig. 7d).

The REE compositions of concordant zircons are shown in Figure 7. Zircons in T01-40 show slightly positively sloped REE profiles with slightly negative Eu anomalies (Fig. 7e). Some zircons show enrichments in Sm to Dy, and there is some minor variation in Lu, however these subtle variations in REE content show no relationship to age. Zircons in T06-09 show flat REE profiles with no Eu anomaly (Fig. 7f).

5.5 Rutile U–Pb geochronology

Isotopic and trace-element data for rutile are in Table A. 6. Analysed rutile grains in both samples were typically 60–100 µm. When imaged in BSE some rutile grains contained fine exsolution of ilmenite, these were avoided. The rutile was analysed in grain mounts, however, in both samples rutile was only observed as inclusions in garnet. Rutile inclusions in garnet were observed in contact with ilmenite, zircon and quartz (Fig. 2). The U–Pb results for T01-40 are shown in Figure 8a (error ellipses are 2σ). Five analyses were omitted due to inclusions being incorporated in the ablation, and six analyses were omitted due to high concentrations of ^{208}Pb (> 0.2 ppm; Fig. B. 3). These high ^{208}Pb analyses define a common lead trend (Fig. B. 3). The remaining 80 analyses define a discordia array, with intercepts at 472.5 ± 15.5 and 1994 ± 57 Ma (MSWD = 2.3). Zr concentrations in the rutile analyses are not correlated to their position on the discordia (Fig. 8a). The rutile U–Pb data from T06-09 are discordant, but due to the low number of analyses (*n* = 10), a discordia and intercept ages cannot be well constrained (Fig. 8b). One analyses from T06-09 was omitted due to contamination. Zr concentrations are not correlated to discordance of the analyses.

5.6 Ti in zircon and Zr in rutile thermometry

In both samples, rutile, quartz and zircon all occur as inclusions within garnet porphyroblasts, and in T01-40 they occur together as multi-mineral inclusions (Fig. 2). As such, it is assumed that these phases were in equilibrium during rutile growth. The results of the thermometry are shown in Figure 9 and summarised in Table 2, Ti contents in zircon and Zr contents in rutile are in Tables A. 5 and A. 6 respectively. Only concordant analyses were used in Ti in zircon calculations, and temperatures were calculated using the Watson & Ferry (2007) calibration. Zircons in T01-40 have Ti contents of 1.1 ± 2 to 17.2 ± 5.2 ppm, with an average of 6.5 ± 2.8 ppm (n = 78; 2σ). These Ti contents correspond to temperatures of 573 ± 127 °C to 799 ± 54 °C, with a mean of 705 ± 9°C (Fig. 9a; 2σ; MSWD = 2.01). Ti contents do not show a relationship with U–Pb date or core/rim location of analysis on zircon (Fig. B. 4). Zircons in T06-09 have Ti contents of 3.4 ± 1.7 to 14.2 ± 3.5 ppm, with an average of 8.6 ± 2.7 ppm (n = 13; 2σ). This corresponds to temperatures of 653 ± 59 °C to 779 ± 51 °C, with a mean of 729 ± 25 °C (Fig. 9b; 2σ; MSWD = 2.33). Ti content, U–Pb date and location of analysis on zircon grain show no relationship (Fig. B. 4).

Temperatures were calculated from Zr contents in rutile using the pressure-dependant calibration of Tomkins et al. (2007). Results are reported at pressures of 10 kbar and 18 kbar, this is done as 10 kbar is the minimum pressure at which rutile is stabilized, and 18 kbar is the interpreted peak pressure from mineral equilibria modelling (see below). Uncertainties on the temperatures were ~5.7 % on average, and were calculated using the quadrature summation of relative errors inherent in the calculations, including 2σ errors on the Zr content (± 1–1.2%), the error associated with the pressure (± 1 kbar), and the error associated with calibration of the thermometer. This was assigned at ± 3% after Watson et al. (2006), as no error is provided in the Tomkins et al. (2007) calibration. In T01-40, all rutile data have Si contents below 3000 ppm, within acceptable limits for eclogitic rutile (Zack et al., 2002), suggesting no incorporation of zircon and/or silicate inclusions. The rutile yields a range of Zr concentrations from 194 ± 2 to 1234 ± 16 ppm (n = 84), corresponding to temperatures of 649 ± 31 °C to 826 ± 48 °C at 18 kbar, with a mean value of 742 ± 7 °C (Fig. 9c; MSWD = 4.31). In T06-09, one rutile analysis was removed due to Si contents of ~ 20,000 ppm. The remaining ten analyses range from 297 ± 5 to 1143 ± 18 ppm Zr, corresponding to temperatures of 683 ± 35 °C to 810 ± 47 °C at 18 kbar, with a mean value of 768 ± 33 °C (Fig. 9d; MSWD = 5.26).

Table 2: *Summary of temperatures calculated from Ti in zircon and Zr in rutile thermometry. Zr in rutile temperatures are reported at both 10 and 18 kbar. This is done as 10 kbar is the minimum pressure at which rutile is stabilized, and 18 kbar is the interpreted peak pressure from mineral equilibria modelling.*

Method		T01-40	T06-09
	Min	573 ± 127 °C	653 ± 59 °C
Ti in zircon	Max	799 ± 54 °C	779 ± 51 °C
	Average	698 ± 59 °C	725 ± 53 °C
	Min	616 ± 29 °C	648 ± 33 °C
Zr in rutile	Max	786 ± 45 °C	771 ± 44 °C
At 10 kbar	Average	713 ± 38 °C	739 ± 42 °C
	Min	649 ± 31 °C	683 ± 35 °C
Zr in rutile	Max	826 ± 48 °C	810 ± 47 °C
At 18 kbar	Average	750 ± 40 °C	777 ± 44 °C

5.7 Mineral equilibria modelling

T01-40 was modelled with H_2O in excess to investigate the stabilised mineral assemblages on the prograde path (Fig. 10a-b). Since dry mafic rocks are notoriously unreactive, the formation of an interpreted peak eclogite-facies mineral assemblage suggests the rock contained adequate free water to promote reactivity until peak conditions. The mineral inclusions in garnet cores from T01-40 include quartz + titanite + plagioclase, which transitions to quartz + rutile + clinopyroxene closer towards the garnet rims, with hornblende and rare epidote inclusions throughout. Plagioclase is stable in the model to ~ 9 kbar, the titanite to rutile transition occurs at ~ 13.5 kbar, epidote is stable from ~7–21 kbar, and hornblende to ~ 18 kbar, and quartz is stable throughout (Fig. 10a). The inclusion assemblage in garnet suggests the sample evolved through this pressure history, however, there are only very broad temperature constraints from the mineral assemblages themselves. The range of compositions of plagioclase inclusions in garnet are outlined in Figure 10b, and are used to constrain the early prograde path to between 550–650 °C at 6–9 kbar. Additionally, the minimum Zr in rutile temperatures are used to constrain the prograde path. This is done as the minimum Zr in rutile temperatures are interpreted to represent the first crystallization of rutile when rutile stability is reached, at approximately 670° C at 13.5 kbar. The prograde path is then interpreted to evolve up pressure and temperature, traversing the range of Zr in rutile temperatures.

Based on the interpreted former presence of omphacite, the peak assemblage is garnet + omphacite + rutile + quartz ± epidote ± H_2O or melt. This assemblage occurs in the same location in both the model calculated with excess water (Fig. 10) and the model calculated with a set water content (Fig. 11). This field is bound down pressure by the appearance of hornblende, at approximately 18 kbar, thus this is a minimum pressure constraint on the peak conditions. The peak temperatures are estimated from maximum Zr in rutile temperatures at approximately 800 °C, which plot in a melt-bearing field (Fig. 11b). There is no mesoscopic evidence that the rock underwent partial melting. However, melt modes in the peak field are low (< 4 %) and as such may not have left any petrological evidence. Thus, the peak conditions are interpreted to be 800 °C at a minimum of 18 kbar.

The peak to retrograde evolution of T01-40 is interpreted using a mineral equilibria model calculated with a set water content (Fig. 11). This water content was determined from the modal proportion of hornblende in the rock, the only water-bearing mineral in the assemblage. The rock is interpreted to track into the garnet + diopside + quartz + hornblende + plagioclase + ilmenite field, which spans a wide range of temperatures (Fig. 11a). The conditions reached in this field are approximately 750 °C and 7 kbar, constrained by titanium in hornblende (*Hb(T)*), and the current modal proportion of garnet (Fig. 11b). The rock may have continued to evolve to conditions of ~ 500 °C and 6 kbar, as recorded by the addition of magnetite to the retrograde assemblage. This is supported by the X_{Fe} composition of garnet rims, labelled as *G(X)R*, which overlap with the range of retrograde diopside $X_{(Fe)}$ compositions. This may reflect re-equilibration of garnet rims with diopside at retrograde conditions (Fig. 11b).

The prograde history of T06-09 is difficult to reconstruct, as the rock does not contain a diverse range of inclusions inside garnet. As such, we present the peak-retrograde evolution of T06-09, as this is well recorded by the retrograde mineralogy. Similar to T01-40, the maximum Zr in rutile temperature plots above the solidus in the garnet + omphacite + rutile + quartz + melt field, which is bound down-pressure by the hornblende-in line (Fig. 12a). There is no overt evidence for partial melting. However, like sample T01-40, melt modes in this field are low (< 3 %) and may not have left any petrological evidence. As such, the peak conditions are interpreted to be 800 °C at a minimum of 18 kbar. The interpreted retrograde field is garnet + diopside + quartz + hornblende + plagioclase + orthopyroxene + ilmenite, which spans a large *P–T* range. The retrograde path is interpreted to reach approximately 750 °C and 8 kbar, where Ti in hornblende (*Hb(T)*) and garnet modes intersect in this field (Fig. 12b). The retrograde evolution may have continued to 500–650 °C and 4–6 kbar, as recorded by the addition of magnetite. This is supported by the X_{Fe} composition of garnet rims (*G(X)R*), which overlap with the range of retrograde diopside $X_{(Fe)}$ compositions, and may record conditions at which garnet rims re-equilibrated with diopside (Fig. 12b).

6. Discussion

6.1. Timing of eclogite-facies metamorphism

Geochronology collected from the two retrogressed eclogite samples suggests that metamorphism took place at ca. 2 Ga, in agreement with previous work (Möller et al., 1995; Collins et al., 2004).

Garnet Lu–Hf geochronology, the first of its kind collected from the Tanzanian retrogressed eclogites, pinpoints the timing of garnet formation in T01-40 to 1994 ± 9 Ma (Fig. 6a). Lu zoning in the garnet is diffuse but slightly elevated in the core, meaning this age probably reflects the average timing of garnet growth (Fig. 4; 5). In T06-09 however, the whole rock analysis does not fall on an isochron with the garnet aliquots. It is possible that the whole rock Lu–Hf ratio has been disturbed or altered by a later event, possibly related to the fine-grained hornblende veins that cross-cut the sample

(Fig. 2). As such, the apparent whole rock-garnet Lu–Hf age may be geologically meaningless. When only the garnet aliquots are included in the isochron age calculation, they give an isochron age of 1959 ± 31 (Fig. 6c). All though this calculated age has a large error, the upper limit of the uncertainty is close to the T01-40 whole rock-garnet isochron age, suggesting the garnets in T06-09 may have grown at a similar time.

Zircon U–Pb geochronology from the retrogressed eclogite samples gives ages dispersed around ca. 2000 Ma for T01-40, and ca. 2010 Ma for T06-09 (Fig. 7). In T01-40, the weighted mean $^{207}Pb/^{206}Pb$ age is ca. 2023 Ma, older than the weighted mean $^{207}Pb/^{235}U$ age of ca. 2007 Ma and the weighted mean $^{206}Pb/^{238}U$ age of ca. 1994 Ma. This disagreement may possibly reflect a subtle combination of common lead and lead loss in the zircons. The lower limit of the weighted mean $^{207}Pb/^{235}U$ age uncertainty is within the garnet Lu–Hf age uncertainty, and the $^{206}Pb/^{238}U$ age is identical to the garnet age. Most zircons show flat to gently positively sloped REE profiles with slightly negative Eu anomalies, and some show humped MREE profiles, however individual age is not correlated with trace-element composition, making in-depth discussion of the zircon REE patterns difficult (Fig. 7). Garnet cores from this sample are enriched in HREEs, and garnet rims show flat or slightly humped REE profiles, similar to patterns in zircon. As such, we interpret the zircon grew in the presence of garnet. Therefore, in T01-40 prograde-peak metamorphism occurred at ca. 1994 Ma as recorded by garnet and supported by zircon. In T06-09, the zircons generally show flat REE profiles with no Eu anomalies, similar to that of garnet in the sample, suggesting the zircons may have grown in the presence of garnet. However, the large uncertainty on the garnet Lu–Hf age means no definite relative age relationship between the zircon and garnet can be stated. Regardless, prograde-peak metamorphism occurred at ca. 2010 Ma in sample T06-09.

Results from rutile geochronology from T01-40 lie on a discordia array, with an upper intercept of 1994 ± 57 Ma (Fig. 8). Rutile texturally occurs as inclusions in garnet, and was likely entrapped during garnet growth. Despite the large uncertainty, it is evident this upper intercept is within uncertainty of the garnet Lu–Hf age, and reflects the timing of rutile growth during high-pressure metamorphism. The lower intercept of 473 ± 16 Ma most likely reflects resetting of the rutile during cooling in the Pan-African event, which affected the East African Orogen (Fritz et al., 2013) that borders and reworks part of the Isimani Suite (Fig. 1a). Rutile grains in T01-40 range from 50–200 μm but are generally ~ 100 μm in diameter. The closure temperature for rutile is proposed to be ~ 520–610 °C for a 100 μm diameter grain at cooling rate of 2–20 °C/Myr (Cherniak, 2000; Vry & Baker, 2006). As such, conditions in the Isimani Suite during the Pan-African event must have reached close to these temperatures. Unlike Pb, Zr concentrations appear comparatively undisturbed by the resetting event (Fig. 8).

6.3. P–T conditions during subduction

The Zr in rutile thermometer requires the assemblage zircon + rutile + quartz to be in equilibrium. This is likely for at least most of the metamorphic evolution, above approximately 10–13 kbar where rutile becomes stable (Fig. 10–12). In both samples, zircon, rutile and quartz occur as inclusions in garnet (Fig. 2), and in T01-40 all three occur as a polyphase inclusion in garnet (Fig. 2f), further supporting this interpretation. The results of the zircon U–Pb geochronology also indicate zircon grew during the metamorphic event that formed the garnet + rutile assemblage in the retrogressed eclogites.

In each sample, rutile is restricted to inclusions in garnet, suggesting the calculated rutile temperatures reflect temperatures during prograde to peak metamorphism. In both T01-40 and T06-09, the $p(\chi^2)$ values for each temperature mean are 0 (Fig. 9). This suggests the spread of temperatures are not within range of the analytical uncertainty. As such, the range of temperatures in each sample are interpreted to reflect the prograde to peak temperatures of rutile crystallization. This requires rutile to be recrystallising and updating its Zr content as it was captured in growing garnet during prograde metamorphism. Mineral equilibria modelling suggests the minimum pressure rutile stabilizes at is approximately 10–13 kbar, and peak pressures reached for each sample were 18 kbar (as a minimum;

Fig. 10–12). In T01-40 the total range of temperatures calculated from 10 to 18 kbar are ~ 615–825 °C, in T06-09 the total range of temperatures calculated from 10 to 18 kbar are ~ 650–810 °C.

Similarly, the range of calculated Ti in zircon temperatures have low $p(\chi^2)$ values, indicating the range may reflect individual crystallization temperatures, and are generally in agreement with the results from Zr in rutile thermometry. In T01-40, the total range of temperatures are ~ 570–800 °C, however as there is no correlation with Ti content and age due to large uncertainties on each spot analysis, it is difficult to establish the relationship between the calculated temperatures and the *P–T* evolution of the retrogressed eclogite. However, it is likely the Ti in zircon temperatures reflect prograde-peak temperatures. In T06-09 the total range of Ti in zircon temperatures are 650–780 °C. As the timing of zircon vs garnet growth is difficult to assess, but zircons in T06-09 have flat REE profiles and appear to have grown with garnet, it is assumed that these temperatures reflect crystallization during prograde metamorphism of the eclogite.

The two samples experienced similar peak *P–T* conditions of approximately 18 kbar and 800 °C, however the pressure estimate is a minimum. The peak mineral assemblage in both samples is interpreted to be hornblende-free, and the peak field is constrained by a hornblende-in line at approximately 18 kbar. It is therefore possible that the retrogressed eclogites reached higher pressures above this line. This may have been preserved in the composition of garnet rims, but these have been resorbed by subsequent retrogression. It may have also been preserved by matrix mineralogy in the form of peak epidote (or its absence), however the matrix has also been significantly reworked. As such, the exact pressures reached by the samples remains unknown, but must have been at least 18 kbar. The retrogressed eclogites experienced similar retrograde conditions of approximately 7–8 kbar and 750 °C, as recorded by the development of retrograde Na-poor clinopyroxene-hornblende and/or orthopyroxene-bearing assemblages. This was possibly followed by cooling to 500 °C at ~ 5 kbar, recorded by the X_{Fe} compositions of the outermost garnet rims and the X_{Fe} of diopside, interpreted to have re-equilibrated at retrograde conditions, and the formation of late-stage magnetite.

The calculated peak conditions recorded by the retrogressed eclogites are similar to published results of approximately 18 kbar and 750 °C (Möller et al., 1995; Brown et al., 2020), although Möller et al. combined texturally retrograde plagioclase with texturally peak metamorphic minerals. The *P*–*T* paths are also similar to those of Brown et al. (2020). The peak *P*–*T* conditions correspond to thermal gradients of 45 °C/kbar, consistent with warm conditions during subduction (e.g. Brown & Johnson, 2018; Agard et al., 2018). These conditions may be a result of warmer ambient mantle temperatures in the Palaeoproterozoic. However, as shown by Ganne & Feng (2017), ambient mantle temperatures at ca. 2000 Ma were probably only marginally warmer than in the late Neoproterozoic when eclogite emerged in the geological record. Therefore, the warm thermal conditions recorded by the Usagaran high-pressure rocks could also potentially reflect slow burial either due to slow subduction rates and/or a shallow subduction angle

6.4. Garnet zoning and thermal histories of the retrogressed eclogites

Despite the similarities in the mineralogy between the two samples, garnets in T01-40 and T06-09 show distinctly different zoning patterns in both major and trace-elements. There is no immediate explanation for why this is the case, as the garnets have experienced similar *P*–*T*–*t* histories and have grown in similar bulk compositions, and hence interacted with similar mineral assemblages. Garnets in all samples show a narrow, resorbed rim, enriched in Y and Lu. Y and Lu zoning in T01-40 show enrichments in the garnet cores, consistent with Rayleigh fractionation during porphyroblast growth (Otamendi et al., 2002), and an enriched annulus close to the rim, probably correlated with breakdown of an accessory mineral during prograde metamorphism (possibly allanite, e.g. Hyppolito et al., 2019). This core enrichment can be seen in garnets of all sizes (~200–1500 µm). Garnets in T06-09 however show either flat Y and Lu profiles in smaller garnets (~ 400 µm across), or depleted Y and Lu cores and progressive enrichments towards the rims in larger garnets (~ 1500 µm across), the inverse of what is seen in garnets of T01-40. Garnets in T06-09 are generally smaller than in T01-40, however small garnets mapped on the edge of the larger garnet in T01-40 show similar patterns to the largest garnets of T01-40 (Fig. 4), negating size as the explanation for these differing patterns across the two samples.

Reverse Rayleigh zoning in HREE elements has been noted, largely in high-pressure rocks (Hickmott & Spear, 1992; Skora et al., 2006; Moore et al., 2013; Maldonado et al., 2018; Hyppolito et al., 2019). This reverse zoning could have been formed during prograde growth, or during diffusional modification of originally Rayleigh-fractionated garnets. The latter would require T06-09 to have resided at high temperatures (> 650 °C) for an extended period of time, resulting in garnets with relatively flat core profiles and enriched resorption rims (e.g. Kelly et al., 2011). However, garnets in T01-09 show a depletion of Y and Lu in their cores, which would require uphill diffusion of these elements towards the edge of the garnet. As this seems unlikely, we postulate the reverse Rayleigh zoning formed as a result of diffusion-limited REE uptake during garnet growth (Skora et al., 2006; Moore et al., 2013). This may have occurred if T06-09 had a lower water content than T01-40, limiting diffusivity of the REE elements through the matrix to the site of garnet growth. The current mineral assemblages in the retrogressed eclogites do not record the amount of water available during prograde metamorphism, however T06-09 currently has 0.2 wt% mineral bound H_2O, compared to T01-40 which currently has 0.35 wt% mineral bound H_2O (Table A. 2). Even though the samples are now retrogressed, it appears likely that T01-40 contained more H_2O than T06-09.

The Cr and V distributions in garnets from the samples show patterns which are not correlated with major or rare earth elements (Fig. 4). Like the REEs, Cr and V have low rates of diffusivity, and their distributions in garnet are usually the result of breakdown of Cr and V bearing minerals, namely amphibole and epidote in mafic rocks (Spandler et al., 2003; Yang & Enami, 2003; Carlson, 2012; Volkova et al., 2014). Garnets in T01-40 and T06-09 have patchy Cr enrichments, in T01-40 these are abundant and elongate, and in T09-09 they are less abundant and equant. The enrichments probably formed due to overgrowth of a pre-existing hornblende foliation (e.g., Yang & Rivers, 2001). In V, small equant enrichments can be seen in garnet in T01-40, and large patchy enrichments can be seen in the garnet in T06-09, suggesting overgrowth of V rich crystals, such as epidote (Yang & Rivers, 2001). Garnets in T01-40 have a sharp rim enriched in both Cr and V, and in T06-09 garnets have a thin irregular rim enriched in Cr. These rims probably formed during final breakdown of hornblende on the prograde path (e.g., Fig. 11; 12).

Major element zoning in garnet has been widely used to infer the thermal histories of metamorphic rocks (e.g. Ganguly et al., 2000; Dachs & Proyer, 2002; Carlson, 2006; Caddick et al., 2010; Spear, 2014). However, this must be done with caution as it requires assumptions about the compositional zoning in garnet prior to diffusional modification. The compositional patterns in garnet in T01-40 and T06-09 during prograde to peak metamorphism are unknown. Currently, garnets in T01-40 have modified prograde zoning in the major elements, preserved as diffuse bell-shaped Mn profiles and Fe and Mg zoning, however garnets in T06-09 preserve flat major element profiles (Fig. 3). Garnets in both samples preserve ~ 50 μm wide rims that are enriched in Mn. These observations hold true in garnets with similar sizes (~1000 μm) across the two samples (Fig. B. 2). If the assumption is made that garnets in T06-09 developed prograde growth zoning similar to garnets in T01-40, this zoning must have been homogenised or flattened by post-growth diffusional relaxation (e.g., Caddick et al., 2010; Carlson, 2012). We note that this may not have been the case. Trace-elements in garnets in T06-09 show diffusion-limited zoning, which may suggest that major elements in T06-09 did not prograde zone in a similar way to T01-40. If diffusional relaxation of any prograde zoning in T06-09 did occur, it must have occurred prior to retrogression and consumption of garnet rims, as the Mn-rich rims in T06-09 are still preserved.

Using Figure 2 of Caddick et al. (2010), the timescale at which diffusion becomes significant can be estimated if the temperature and diffusion length-scale are known. Maximum peak temperatures are estimated to be ~ 800 °C for both of the samples. The average preserved diameter of garnets T06-09 is ~1000 μm. Thus, for T06-09 to flatten any major element zoning, it must have remained at 800 °C for at least 6 Myr. Garnets ~ 1000 μm in diameter in T01-40 retain a vestige of their major element zoning, but record similar peak temperatures to T06-09 (Fig. 3, Fig. B. 2). T01-40 also is likely to have undergone diffusion of major elements, as the zonation patterns in Mn, Fe and Mg are diffuse. However, it has experienced less homogenisation than T06-09.

If the above is true, sample T01-40 and T06-09 may have recorded different thermal histories. The simplest explanation is that T06-09 may have been stalled at depth above the closure temperature for major element diffusion in garnet during peak metamorphism for at least 6 Myr, while T01-40 was immediately exhumed to depths below the closure temperature of major element diffusion in garnet. T01-40 and T06-09 are sampled from ~ 5 km of each other (Fig. 1b), however are separated by > 100 meters of amphibolite-facies shear zones. It is possible that T01-40 was exhumed immediately to shallower crustal levels and thus lower temperatures and pressures than T06-09 following peak metamorphism via these shear zones.

6.5. Tectonic model for formation of the Usagaran retrogressed eclogites

The current tectonic model for metamorphism of the Usagaran retrogressed eclogites and the Isimani Suite involves subduction of the Tanzanian margin (Möller et al., 1995; Ring et al., 1997; Reddy et al., 2003; Collins et al., 2004). The MORB-like composition of the retrogressed eclogites has led authors to suggest subduction of either oceanic crust or mafic intrusions in a marginal basin (Möller et al., 1995; Reddy et al., 2003). The existence of Archean and Palaeoproterozoic crust immediately adjacent to the Usagaran Belt in the reworked Mozambique Belt, as well as the abundance of continental and felsic material in the Isimani Suite, has led to the suggestion that a small microcontinent or continental ribbon was rifted off the Tanzanian Craton prior to formation of the Usagaran eclogites (Maboko et al., 2000; Muhongo et al., 2001; Reddy et al., 2003; Sommer et al., 2005b). Subduction has been interpreted as east-dipping, based on the presence of Palaeoproterozoic amphibolite-facies east-dipping fabrics in the Isimani Suite (Reddy et al., 2003). This basin was then subducted under the continental ribbon at ca. 2000 Ma, and then exhumed in a transpressional regime during docking of the ribbon on the margin of the craton. Brown et al. (2020) suggested the retrogressed eclogites were exhumed in an extensional regime after slab breakoff and buoyancy driven exhumation, a more likely driver of exhumation of high-pressure rocks from mantle depths (e.g. Sizova et al., 2014; Petersen & Buck, 2015). This was supported by the fact that the east-dipping fabrics in the Isimani Suite are shallowly dipping, a feature often indicative of extension or transtention (Reddy et al., 2003; Brown et al., 2020). I-type granitoids and volcanics which intruded the Usagaran Belt between ca. 1940 and 1870 Ma are interpreted to be subduction related, calling for continued subduction of oceanic crust for up to ca. 130 Myr after metamorphism of the Usagaran retrogressed eclogites (Maboko & Nakamura, 1996; Reddy et al., 2003; Sommer et al., 2005a; Bahame et al., 2016).

We postulate two likely tectonic scenarios for subduction and exhumation of the Usagaran retrogressed eclogites and the Isimani Suite (Fig. 13). The primary difference between the models is the polarity of subduction during eclogite-facies metamorphism. The first scenario is similar to that of previous workers (Möller et al., 1995; Ring et al., 1997; Reddy et al., 2003; Collins et al., 2004). It involves east-dipping subduction of oceanic crust on the margin of the Tanzanian Craton under a possible continental ribbon (Fig. 13a). The Isimani Suite metapelitic and felsic gneisses formed in an accretionary wedge, which is sourced from both the Tanzanian Craton and possibly the ribbon (Collins et al., 2004). Metamorphism of the retrogressed eclogites occurred from ca. 2010–1994 Ma, and they reached pressures of at least 18 kbar. Within at least 6 Myr, slab breakoff resulted in buoyancy-driven exhumation of the mafic eclogites, which were incorporated into the metapelitic gneisses (Fig. 13b; e.g. Petersen & Buck, 2015). Following this, subduction polarity was flipped, and oceanic crust began to subduct under the ribbon (Reddy et al., 2003). The exhumed oceanic crust and accretionary material of the Isimani Suite then became part of an extensional back arc system (Fig. 13e). At this point, the retrogressed eclogites were feasibly at shallow crustal levels, and had been exhumed by further extension and formation of shallowly east-dipping fabrics in the Isimani Suite (Reddy et al., 2003; Brown et al., 2020).

The above model accounts for the geology of the Usagaran Belt, however, there is another tectonic scenario which is also possible for formation and exhumation of the Usagaran eclogites (Fig. 13c-d).

This scenario involves west-dipping subduction of oceanic crust under the margin of the Tanzanian Craton, where the mafic eclogites and encasing Isimani gneisses were metamorphosed from ca. 2010–1994 Ma (Fig. 13c). While west-dipping subduction under the Tanzanian Craton has not been suggested for formation of the eclogites before, it does align with ca. 2 Ga metasomatic mantle enrichments under the craton in the northern Usagaran Belt, which were probably formed from subduction related fluids (Konreef et al., 2009; Aulbach et al., 2011). Buoyancy-driven exhumation of the retrogressed eclogites occurred immediately (within ca. 6 Myr) after peak conditions, and the continental ribbon was docked onto the margin of the Isimani Suite (Fig. 13d). This resulted in stepping back of the subduction zone, which placed the Isimani Suite into an extensional back arc basin, possibly aiding in exhuming the retrogressed eclogites to shallow crustal levels (Fig. 13e).

After exhumation of the eclogites, the tectonic evolution of the Usagaran Belt above a west-dipping subduction zone is the same in both models (Fig. 13e-f). Thinning of the basement oceanic crust in the back arc basin led to the deposition of the Konse Group sediments, and the extrusion of pillow basalts with back arc affinities into these sediments (Fig. 13e; Boniface & Tsujimori, 2018). This occurred between ca. 1990–1920 Ma. Continued west-dipping subduction of oceanic crust resulted in intrusion of post-tectonic granitoids and the Ndembera group volcanics, interpreted to be arc related, into the Usagaran Belt from ca. 1940–1870 Ma (Fig. 13f; Sommer et al., 2005a; Bahame et al., 2016).

The newly suggested scenario for formation and exhumation of the high-pressure rocks is similar to that of the Ordovician–Silurian Western Gneiss Complex in Norway (Hacker et al., 2003; Kylander-Clark et al., 2008; Hacker et al., 2010). Following high pressure metamorphism and slab breakoff, the subducted crust buoyantly exhumed into the upper plate (Hacker et al., 2010). As the subduction zone stepped back, further exhumation occurred along extensional detachments in a back arc system. *P*–*T* paths during exhumation of the Western Gneiss Complex eclogites were isothermal, resulting in amphibolite-facies overprinting of the mafic eclogites, similar to that recorded by the Usagaran retrogressed eclogites (Walsh & Hacker, 2004). While it is not possible to distinguish between the two tectonic models that led to the formation of the high-pressure rocks and evolution of the Usagaran Belt, it is evident that slab breakoff, buoyant rise of the underlying plate and its conversion to a back arc system were integral in exhuming the eclogites of the Isimani Suite.

7. Conclusions

Retrogressed eclogites from Yalumba Hill in the Usagaran Belt preserve evidence for subduction related eclogite-facies metamorphism. Garnet growth is dated by Lu–Hf at ca. 1994 Ma in one of the samples, and is supported by zircon U–Pb geochronology dispersed around ca. 2000 Ma. Rutile U–Pb geochronology from the same sample yields an upper intercept of ca. 1994 Ma, supporting eclogite-facies metamorphism at this time. Zr in rutile thermometry and mineral equilibria modelling suggest the eclogites reached 800 °C and at least 18 kbar, and were retrogressed to conditions of approximately 7–8 kbar and 750 °C. This corresponds to thermal gradients of ~ 45 °C/kbar, consistent with warm conditions during subduction. These warm conditions may have been the result of a warmer mantle temperature in the Palaeoproterozoic, and shallow, low-angle subduction. Tectonic models for formation and exhumation of the retrogressed eclogites involve either east-dipping subduction of oceanic crust on the Tanzanian Craton margin, or, west-dipping subduction of oceanic crust under the Tanzanian Craton. Buoyancy driven exhumation of the retrogressed eclogites occurred after slab breakoff, followed by a subduction polarity switch or a step back in the subduction zone, which placed the eclogites and Isimani Suite into a back-arc position. The similarity in age and *P*–*T* conditions of the Usagaran retrogressed eclogites with eclogites from the Eburnian-Transamazonian and Ubende orogens demonstrates that a large subduction system may have been stable on the margin of the Tanzanian Craton from ca. 2.1–1.9 Ga. This suggests that modern style subduction was operating on significant geographic and temporal scales by this time in Earth's history.

Acknowledgements

We are grateful to Sarah Gilbert, Ben Wade and Aoife McFadden of Adelaide Microscopy for their assistance with data collection. Alan Collins is thanked for providing sample T01-40. We thank Dariusz Sala, Milena Matyszczak, Martyna Rogozik and Maria Repczyńska for their assistance with Lu–Hf data collection. David Kelsey and Jack Gillespie are thanked for helpful discussions. We thank Andrew Kylander-Clark and an anonymous reviewer for their helpful comments on the manuscript, and Marco Scambelluri for his editorial handling. The authors acknowledge financial support from the Australian Research Council (ARC) grant h. Renée Tamblyn acknowledges financial support from the Aldermann Kleeman travel scholarship from the University of Adelaide.

References:

Agard, P., Plunder, A., Angiboust, S., Bonnet, G., & Ruh, J. (2018). The subduction plate interface: Rock record and mechanical coupling (from long to short time scales). *Lithos*.

Anczkiewicz, R., Platt, J. P., Thirlwall, M. F., & Wakabayashi, J. (2004). Franciscan subduction off to a slow start: evidence from high-precision Lu–Hf garnet ages on high grade-blocks. *Earth and Planetary Science Letters, 225*(1), 147-161.

Anczkiewicz, R., & Thirlwall, M. F. (2003). Improving precision of Sm-Nd garnet dating by H2SO4 leaching: a simple solution to the phosphate inclusion problem. *Geological Society, London, Special Publications, 220*(1), 83-91.

Aulbach, S., Rudnick, R. L., & McDonough, W. F. (2011). Evolution of the lithospheric mantle beneath the East African Rift in Tanzania and its potential signatures in rift magmas. *Geological Society of America Bulletin, 478*, 105-125.

Bahame, G., Manya, S., & Maboko, M. A. (2016). Age and geochemistry of coeval felsic volcanism and plutonism in the Palaeoproterozoic Ndembera Group of southwestern Tanzania: Constraints from SHRIMP U–Pb zircon and Sm–Nd data. *Precambrian Research, 272*, 115-132.

Baldwin, J. A., Bowring, S. A., Williams, M. L., & Williams, I. S. (2004). Eclogites of the Snowbird tectonic zone: petrological and U-Pb geochronological evidence for Paleoproterozoic high-pressure metamorphism in the western Canadian Shield. *Contributions to Mineralogy and Petrology, 147*(5), 528-548.

Boniface, N., Schenk, V., & Appel, P. (2012). Paleoproterozoic eclogites of MORB-type chemistry and three Proterozoic orogenic cycles in the Ubendian Belt (Tanzania): Evidence from monazite and zircon geochronology, and geochemistry. *Precambrian Research, 192*, 16-33.

Boniface, N., & Tsujimori, T. (2019). Pillow lava basalts with back-arc MORB affinity from the Usagaran Belt, Tanzania: relics of Orosirian ophiolites. *Journal of the Geological Society, 176*(5), 1007-1021.

Bradley, D. C. (2011). Secular trends in the geologic record and the supercontinent cycle. *Earth-Science Reviews, 108*(1-2), 16-33.

Brick, R. A. (2011). *Palaeoproterozoic eclogite formation in Tanzania: a structural, geochronological, thermochronological and metamorphic study of the Usagaran and Ubende orogenic belts.*

Brown, D. A., Tamblyn, R., Hand, M., & Morrissey, L. J. (2020). Thermobarometric constraints on burial and exhumation of 2-billion-year-old eclogites and their metapelitic hosts. *Precambrian Research*, 105833.

Brown, M., & Johnson, T. (2018). Secular change in metamorphism and the onset of global plate tectonics. *American Mineralogist, 103*(2), 181-196.

Caddick, M. J., Konopásek, J., & Thompson, A. B. (2010). Preservation of garnet growth zoning and the duration of prograde metamorphism. *Journal of Petrology, 51*(11), 2327-2347.

Carlson, W. D. (2012). Rates and mechanism of Y, REE, and Cr diffusion in garnet. *American Mineralogist, 97*(10), 1598-1618.

Cherniak, D. (2000). Pb diffusion in rutile. *Contributions to Mineralogy and Petrology, 139*(2), 198-207.

Collins, A. S., Reddy, S. M., Buchan, C., & Mruma, A. (2004). Temporal constraints on Palaeoproterozoic eclogite formation and exhumation (Usagaran Orogen, Tanzania). *Earth and Planetary Science Letters, 224*(1-2), 175-192.

Corfu, F., Hanchar, J. M., Hoskin, P. W., & Kinny, P. (2003). Atlas of zircon textures. *Reviews in mineralogy and geochemistry, 53*(1), 469-500.

Dachs, E., & Proyer, A. (2002). Constraints on the duration of high-pressure metamorphism in the Tauern Window from diffusion modelling of discontinuous growth zones in eclogite garnet. *Journal of metamorphic Geology, 20*(8), 769-780.

Droop, G. (1987). A general equation for estimating Fe3+ concentrations in ferromagnesian silicates and oxides from microprobe analyses, using stoichiometric criteria. *Mineralogical Magazine, 51*(361), 431-435.

Elburg, M., Bons, P., Foden, J., & Brugger, J. (2003). A newly defined Late Ordovician magmatic-thermal event in the Mt Painter Province, northern Flinders Ranges, South Australia. *Australian Journal of Earth Sciences, 50*(4), 611-631.

Ferry, J., & Watson, E. (2007). New thermodynamic models and revised calibrations for the Ti-in-zircon and Zr-in-rutile thermometers. *Contributions to Mineralogy and Petrology, 154*(4), 429-437.

François, C., Debaille, V., Paquette, J.-L., Baudet, D., & Javaux, E. J. (2018). The earliest evidence for modern-style plate tectonics recorded by HP–LT metamorphism in the Paleoproterozoic of the Democratic Republic of the Congo. *Scientific reports, 8*(1), 1-10.

Fritz, H., Abdelsalam, M., Ali, K., Bingen, B., Collins, A., Fowler, A., Ghebreab, W., Hauzenberger, C., Johnson, P., & Kusky, T. (2013). Orogen styles in the East African Orogen: A review of the Neoproterozoic to Cambrian tectonic evolution. *Journal of African Earth Sciences, 86*, 65-106.

Ganguly, J., Dasgupta, S., Cheng, W., & Neogi, S. (2000). Exhumation history of a section of the Sikkim Himalayas, India: records in the metamorphic mineral equilibria and compositional zoning of garnet. *Earth and Planetary Science Letters, 183*(3-4), 471-486.

Ganne, J., & Feng, X. (2017). Primary magmas and mantle temperatures through time. *Geochemistry, Geophysics, Geosystems, 18*(3), 872-888.

Green, E., White, R., Diener, J., Powell, R., Holland, T., & Palin, R. (2016). Activity–composition relations for the calculation of partial melting equilibria in metabasic rocks. *Journal of metamorphic Geology, 34*(9), 845-869.

Hacker, B., Andersen, T., Root, D., Mehl, L., Mattinson, J., & Wooden, J. (2003). Exhumation of high-pressure rocks beneath the Solund Basin, western gneiss region of Norway. *Journal of metamorphic Geology, 21*(6), 613-629.

Hacker, B. R., Andersen, T. B., Johnston, S., Kylander-Clark, A. R., Peterman, E. M., Walsh, E. O., & Young, D. (2010). High-temperature deformation during continental-margin subduction & exhumation: The ultrahigh-pressure Western Gneiss Region of Norway. *Tectonophysics, 480*(1-4), 149-171.

Herms, P. (2002). Fluids in a 2 Ga old subduction zone—deduced from eclogite-facies rocks of the Usagaran belt, Tanzania. *European Journal of Mineralogy, 14*(2), 361-373.

Herwartz, D., Skublov, S., Berezin, A., & Mel'Nik, A. (2012). *First Lu-Hf garnet ages of eclogites from the Belomorian mobile belt (Baltic shield, Russia).* Paper presented at the Doklady Earth Sciences.

HICKMOTT, D., & SPEAR, F. S. (1992). Major-and trace-element zoning in garnets from calcareous pelites in the NW Shelburne Falls Quadrangle, Massachusetts: garnet growth histories in retrograded rocks. *Journal of Petrology, 33*(5), 965-1005.

Holland, T., & Powell, R. (2011). An improved and extended internally consistent thermodynamic dataset for phases of petrological interest, involving a new equation of state for solids. *Journal of metamorphic Geology, 29*(3), 333-383.

Hyppolito, T., Cambeses, A., Angiboust, S., Raimondo, T., García-Casco, A., & Juliani, C. (2019). Rehydration of eclogites and garnet-replacement processes during exhumation in the amphibolite-facies. *Geological Society, London, Special Publications, 478*(1), 217-239.

Jackson, S. E., Pearson, N. J., Griffin, W. L., & Belousova, E. A. (2004). The application of laser ablation-inductively coupled plasma-mass spectrometry to in situ U–Pb zircon geochronology. *Chemical geology*, *211*(1-2), 47-69.

Jackson, S. E., Pearson, N. J., Griffin, W. L., & Belousova, E. A. (2004). The application of laser ablation-inductively coupled plasma-mass spectrometry to in situ U–Pb zircon geochronology. *Chemical geology*, *211*(1-2), 47-69.

Jochum, K. P., Weis, U., Stoll, B., Kuzmin, D., Yang, Q., Raczek, I., Jacob, D. E., Stracke, A., Birbaum, K., & Frick, D. A. (2011). Determination of reference values for NIST SRM 610–617 glasses following ISO guidelines. *Geostandards and Geoanalytical Research*, *35*(4), 397-429.

Janoušek, V., Farrow, C. M., & Erban, V. (2006). Interpretation of whole-rock geochemical data in igneous geochemistry: introducing Geochemical Data Toolkit (GCDkit). *Journal of Petrology*, *47*(6), 1255-1259.

Kelly, E., Carlson, W. D., & Connelly, J. (2011). Implications of garnet resorption for the Lu–Hf garnet geochronometer: an example from the contact aureole of the Makhavinekh Lake Pluton, Labrador. *Journal of metamorphic Geology, 29*(8), 901-916.

Konrad-Schmolke, M., Zack, T., O'Brien, P. J., & Jacob, D. E. (2008). Combined thermodynamic and rare earth element modelling of garnet growth during subduction: examples from ultrahigh-pressure eclogite of the Western Gneiss Region, Norway. *Earth and Planetary Science Letters*, *272*(1-2), 488-498.

Koornneef, J. M., Davies, G. R., Döpp, S. P., Vukmanovic, Z., Nikogosian, I. K., & Mason, P. R. (2009). Nature and timing of multiple metasomatic events in the sub-cratonic lithosphere beneath Labait, Tanzania. *Lithos, 112*, 896-912.

Kylander-Clark, A., Hacker, B., & Mattinson, J. (2008). Slow exhumation of UHP terranes: titanite and rutile ages of the Western Gneiss Region, Norway. *Earth and Planetary Science Letters, 272*(3-4), 531-540.

Kylander-Clark, A. R., Hacker, B. R., Johnson, C. M., Beard, B. L., & Mahlen, N. J. (2009). Slow subduction of a thick ultrahigh-pressure terrane. *Tectonics, 28*(2).

Liu, Y., Hu, Z., Zong, K., Gao, C., Gao, S., Xu, J., & Chen, H. (2010). Reappraisement and refinement of zircon U-Pb isotope and trace element analyses by LA-ICP-MS. *Chinese Science Bulletin*, *55*(15), 1535-1546.

Liu, F., Zhang, L., Li, X., Slabunov, A. I., Wei, C., & Bader, T. (2017). The metamorphic evolution of Paleoproterozoic eclogites in Kuru-Vaara, northern Belomorian Province, Russia: Constraints from PT pseudosections and zircon dating. *Precambrian Research, 289*, 31-47.

Locock, A. J. (2014). An Excel spreadsheet to classify chemical analyses of amphiboles following the IMA 2012 recommendations. *Computers & Geosciences, 62*, 1-11.

Loose, D., & Schenk, V. (2018). 2.09 Ga old eclogites in the Eburnian-Transamazonian orogen of southern Cameroon: Significance for Palaeoproterozoic plate tectonics. *Precambrian Research*, *304*, 1-11.

Luvizotto, G., Zack, T., Meyer, H., Ludwig, T., Triebold, S., Kronz, A., Münker, C., Stockli, D., Prowatke, S., & Klemme, S. (2009). Rutile crystals as potential trace-element and isotope mineral standards for microanalysis. *Chemical Geology, 261*(3-4), 346-369.

Maboko, M. A. (2000). Nd and Sr isotopic investigation of the Archean–Proterozoic boundary in north eastern Tanzania: constraints on the nature of Neoproterozoic tectonism in the Mozambique Belt. *Precambrian Research, 102*(1-2), 87-98.

Maboko, M. A., & Nakamura, E. (1996). Nd and Sr isotopic mapping of the Archaean-Proterozoic boundary in southeastern Tanzania using granites as probes for crustal growth. *Precambrian Research*, *77*(1-2), 105-115.

Maldonado, R., Weber, B., Ortega-Gutiérrez, F., & Solari, L. A. (2018). High-pressure metamorphic evolution of eclogite and associated metapelite from the Chuacús complex (Guatemala Suture Zone): Constraints from phase equilibria modelling coupled with Lu-Hf and U-Pb geochronology. *Journal of metamorphic Geology, 36*(1), 95-124.

Möller, A., Appel, P., Mezger, K., & Schenk, V. (1995). Evidence for a 2 Ga subduction zone: eclogites in the Usagaran belt of Tanzania. *Geology, 23*(12), 1067-1070.

Moore, S., Carlson, W. D., & Hesse, M. A. (2013). Origins of yttrium and rare earth element distributions in metamorphic garnet. *Journal of metamorphic Geology, 31*(6), 663-689.

Mori, K., Tsujimori, T., & Boniface, N. (2018). Finding of talc–and kyanite–bearing amphibolite from the Paleoproterozoic Usagaran Belt, Tanzania. *Journal of Mineralogical and Petrological Sciences, 113*(6), 316-321.

Mruma, A. (1989). *Stratigraphy, Metamorphism and Tectonic Evolution of the Early Proterozoic Usagaran Belt, Tanzania.* (Ph.D), University of Oulu, Finland.

Muhongo, S., Kröner, A., & Nemchin, A. (2001). Single zircon evaporation and SHRIMP ages for granulite-facies rocks in the Mozambique Belt of Tanzania. *The Journal of Geology, 109*(2), 171-189.

Müller, S., Dziggel, A., Sindern, S., Kokfelt, T. F., Gerdes, A., & Kolb, J. (2018). Age and temperature-time evolution of retrogressed eclogite-facies rocks in the Paleoproterozoic Nagssugtoqidian Orogen, South-East Greenland: Constrained from U-Pb dating of zircon, monazite, titanite and rutile. *Precambrian Research, 314*, 468-486.

Otamendi, J. E., de La Rosa, J. D., Douce, A. E. P. o., & Castro, A. (2002). Rayleigh fractionation of heavy rare earths and yttrium during metamorphic garnet growth. *Geology, 30*(2), 159-162.

Palin, R. M., Santosh, M., Cao, W., Li, S.-S., Hernández-Uribe, D., & Parsons, A. (2020). Secular metamorphic change and the onset of plate tectonics. *Earth-Science Reviews*, 103172.

Paton, C., Hellstrom, J., Paul, B., Woodhead, J., & Hergt, J. (2011). Iolite: Freeware for the visualisation and processing of mass spectrometric data. *Journal of Analytical Atomic Spectrometry*, *26*(12), 2508-2518.

Petersen, K. D., & Buck, W. R. (2015). Eduction, extension, and exhumation of ultrahigh-pressure rocks in metamorphic core complexes due to subduction initiation. *Geochemistry, Geophysics, Geosystems, 16*(8), 2564-2581.

Reddy, S. M., Collins, A. S., & Mruma, A. (2003). Complex high-strain deformation in the Usagaran Orogen, Tanzania: structural setting of Palaeoproterozoic eclogites. *Tectonophysics, 375*(1-4), 101-123.

Ring, U., Kröner, A., & Toulkeridis, T. (1997). Palaeoproterozoic granulite-facies metamorphism and granitoid intrusions in the Ubendian-Usagaran Orogen of northern Malawi, east-central Africa. *Precambrian Research, 85*(1-2), 27-51.

Rubatto, D. (2002). Zircon trace-element geochemistry: partitioning with garnet and the link between U–Pb ages and metamorphism. *Chemical Geology, 184*(1-2), 123-138.

Rubatto, D., & Hermann, J. r. (2007). Zircon behaviour in deeply subducted rocks. *Elements, 3*(1), 31-35.

Sizova, E., Gerya, T., & Brown, M. (2014). Contrasting styles of Phanerozoic and Precambrian continental collision. *Gondwana Research, 25*(2), 522-545.

Skora, S., Baumgartner, L. P., Mahlen, N. J., Johnson, C. M., Pilet, S., & Hellebrand, E. (2006). Diffusion-limited REE uptake by eclogite garnets and its consequences for Lu–Hf and Sm–Nd geochronology. *Contributions to Mineralogy and Petrology, 152*(6), 703-720.

Sláma, J., Košler, J., Condon, D. J., Crowley, J. L., Gerdes, A., Hanchar, J. M., ... & Schaltegger, U. (2008). Plešovice zircon—a new natural reference material for U–Pb and Hf isotopic microanalysis. *Chemical Geology, 249*(1-2), 1-35.

Sommer, H., Kröner, A., Hauzenberger, C., & Muhongo, S. (2005). Reworking of Archaean and Palaeoproterozoic crust in the Mozambique belt of central Tanzania as documented by SHRIMP zircon geochronology. *Journal of African Earth Sciences, 43*(4), 447-463.

Sommer, H., Kröner, A., Muhongo, S., & Hauzenberger, C. (2005). SHRIMP zircon ages for post-Usagaran granitoid and rhyolitic rocks from the Palaeoproterozoic terrain of southwestern Tanzania. *South African Journal of Geology, 108*(2), 247-256.

Spandler, C., Hammerli, J., Sha, P., Hilbert-Wolf, H., Hu, Y., Roberts, E., & Schmitz, M. (2016). MKED1: a new titanite standard for in situ analysis of Sm–Nd isotopes and U–Pb geochronology. *Chemical Geology, 425*, 110-126.

Spear, F. (2014). The duration of near-peak metamorphism from diffusion modelling of garnet zoning. *Journal of metamorphic Geology, 32*(8), 903-914.

Stern, R. A., Bodorkos, S., Kamo, S. L., Hickman, A. H., & Corfu, F. (2009). Measurement of SIMS instrumental mass fractionation of Pb isotopes during zircon dating. *Geostandards and Geoanalytical Research, 33*(2), 145-168.

Stern, R. A., Bodorkos, S., Kamo, S. L., Hickman, A. H., & Corfu, F. (2009). Measurement of SIMS instrumental mass fractionation of Pb isotopes during zircon dating. *Geostandards and Geoanalytical Research*, *33*(2), 145-168.

Tomkins, H., Powell, R., & Ellis, D. (2007). The pressure dependence of the zirconium-in-rutile thermometer. *Journal of metamorphic Geology*, *25*(6), 703-713.

Vermeesch, P. (2018). IsoplotR: a free and open toolbox for geochronology. *Geoscience Frontiers, 9*(5), 1479-1493.

Vry, J. K., & Baker, J. A. (2006). LA-MC-ICPMS Pb–Pb dating of rutile from slowly cooled granulites: confirmation of the high closure temperature for Pb diffusion in rutile. *Geochimica et Cosmochimica Acta*, *70*(7), 1807-1820.

Watson, E., Wark, D., & Thomas, J. (2006). Crystallization thermometers for zircon and rutile. *Contributions to Mineralogy and Petrology, 151*(4), 413.

Weller, O., & St-Onge, M. (2017). Record of modern-style plate tectonics in the Palaeoproterozoic Trans-Hudson orogen. *Nature Geoscience, 10*(4), 305-311.

Wiedenbeck, M. A. P. C., Alle, P., Corfu, F., Griffin, W. L., Meier, M., Oberli, F. V., ... & Spiegel, W. (1995). Three natural zircon standards for U-Th-Pb, Lu-Hf, trace-element and REE analyses. *Geostandards newsletter*, *19*(1), 1-23.

Yang, J.-J., & Enami, M. (2003). Chromian dissakisite-(Ce) in a garnet lherzolite from the Chinese Su-Lu UHP metamorphic terrane: Implications for Cr incorporation in epidote-group minerals and recycling of REE into the Earth’s mantle. *American Mineralogist*, *88*(4), 604-610.

Yang, P., & Rivers, T. (2001). Chromium and manganese zoning in pelitic garnet and kyanite: Spiral, overprint, and oscillatory (?) zoning patterns and the role of growth rate. *Journal of metamorphic Geology*, *19*(4), 455-474.

Yu, H., Zhang, L., Lanari, P., Rubatto, D., & Li, X. (2019). Garnet LuHf geochronology and PT path of the Gridino-type eclogite in the Belomorian Province, Russia. *Lithos, 326,* 313-326.

Xu, C., Kynický, J., Song, W., Tao, R., Lü, Z., Li, Y., ... & Fei, Y. (2018). Cold deep subduction recorded by remnants of a Paleoproterozoic carbonated slab. *Nature communications*, *9*(1), 1-8.

Zack, T., Stockli, D. F., Luvizotto, G. L., Barth, M. G., Belousova, E., Wolfe, M. R., & Hinton, R. W. (2011). In situ U–Pb rutile dating by LA-ICP-MS: 208 Pb correction and prospects for geological applications. *Contributions to Mineralogy and Petrology, 162*(3), 515-530.

Figure captions:

Figure 1: a) Geological map of central Tanzania, the Usagaran Belt is located on the eastern margin of the Tanzanian Craton. Location of map (b) is shown in dotted black line. **b)** Geological map of Yalumba Hill and the Ruaha River section in the Usagaran Belt, modified from Brown et al. (2020), Reddy et al. (2003) and Mruma (1989). Locations of samples T01-40 and T06-09 from this study are indicated.

Figure 2: Photomicrographs and BSE images of retrogressed eclogites. **a)** Garnet in T01-40 with titanite and rutile inclusions. **b)**. Coarse-grained garnet in T01-40 with plagioclase and hornblende symplectites forming coronae on its margin. **c)** Garnet in T01-40 with coronae of plagioclase and ilmenite/magnetite. Coarse-grained diopside grains with lamellae of plagioclase and opaques are separated from the garnet by coronae of plagioclase. Hornblende is interpreted to have replaced clinopyroxene along the grain margins. **d)** Symplectitic clinopyroxene in T01-40, the colourless inclusions in the clinopyroxene are plagioclase and opaque inclusions are magnetite, interpreted to have exsolved from a previous Na-rich clinopyroxene. Hornblende is interpreted to have replaced clinopyroxene on the grain margins. **e)** SEM image of a multiphase inclusion of hornblende, plagioclase, rutile and clinopyroxene in garnet from T01-40. The rutile has exsolved fine lamellae of ilmenite. **f)** SEM image of rutile, zircon and quartz included in garnet in T01-40. **g)** Irregular-shaped garnet in T06-09, separated from clinopyroxene by double coronae of plagioclase and hornblende. **h)** Symplectitic clinopyroxene in T06-09, colourless inclusions in the clinopyroxene are plagioclase and opaque inclusions are ilmenite, interpreted to have exsolved from a previous Na-rich clinopyroxene. **i)** Garnet in T06-09, containing clouds of very fine-grained inclusions, which are primarily quartz. The

garnet is surrounded by a corona of plagioclase with symplectic intergrowths of ilmenite and magnetite. Fine grained orthopyroxene has replaced clinopyroxene. **j)** A coarse hornblende grain cross-cutting the mineral assemblages in T06-09. The hornblende primarily replaced clinopyroxene. **k)** SEM images of rare hornblende, plagioclase, quartz, rutile and ilmenite inclusions in garnet from T06-09. **l)** Fine-grained zircon, quartz and hornblende inclusions in garnet from T06-09. Abbreviations: Cpx: Clinopyroxene, G: Garnet, Hb: Hornblende; Ilm: Ilmenite, Mt: Magnetite; Opx: Orthopyroxene, Pl: Plagioclase, Q: Quartz, Ru: Rutile; Ttn: Titanite, Zrc: Zircon.

Figure 3: EPMA maps and traverses of representative garnets from the samples. Note that $X_{(Fe)}$ is plotted on a different axis and the scale changes between the two traverses. **a)** Maps of a garnet from T01-40, showing prograde zoning in the garnet core and 50–100 µm wide re-equilibrated rim. **b)** Maps of a garnet in T06-09, showing flat profiles in the garnet core and a 50–100 µm re-equilibrated rim. **c)** Traverse from garnet in T01-40. **d)** Traverse from garnet in T06-09.

Figure 4: Selected major and trace-element maps for garnets in the retrogressed eclogites. Mn is shown for reference. White dashed lines represent trend of overgrown foliation. White arrows indicate locations of Cr and V rich overgrowths. **a-j)** Maps from two different sized garnets in T01-40. **k-t)** Maps from two different sized garnets in T06-09.

Figure 5: Chondrite normalised REE plots of single garnets. **a)** Garnet from T01-40, showing decreasing HREE and increasing MREE content from core to rim. **b)** Garnet from T06-09, showing a flat REE profile with only subtle change from core to rim.

Figure 6: Lu–Hf isochrons, yellow shading represents the uncertainty on the isochron. **a)** Sample T01-40, showing the whole rock and three garnet aliquots that lie on an isochron. The Model 1 age is calculated as a maximum likelihood regression, taking into account the analytical uncertainties and error correlations, under the assumption that the error is caused by the analytical uncertainty. **b)** Sample T06-09, the Model 3 age is calculated as a maximum likelihood regression with

overdispersion, which may be interpreted as analytical or geological, however the apparent age may not be meaningful**.** **c)** Garnet aliquots only from T06-09, there is a large uncertainty on the calculated Model 1 age due to the restricted range of $^{176}Lu/^{177}Hf$ ratios.

Figure 7: U–Pb and REE results and representative CL images of zircons from the retrogressed eclogites. Empty ellipses are discordant and were omitted from the age calculations. **a)** Concordia plot of data from T01-40. **b)** Concordia plot of data from T06-09. **c)** $^{207}Pb/^{206}Pb$ weighted mean plot of concordant data from T01-40. **d)** $^{207}Pb/^{206}Pb$ weighted mean plot of concordant data from T06-09. **e)** REE of zircons normalised to chondrite in T01-40. **f)** REE of zircons normalised to chondrite in T06-09.

Figure 8: Rutile U–Pb results. Ellipses are colour-coded for Zr content. Omitted analyses are in Figure. B. 3. Error ellipses are 2σ. **a)** Rutile from T01-40, defining a discordia between ca. 1994 and 473 Ma. Zr content is not correlated with the resetting of rutile grains. **b)** Rutile from T06-09, lack of data means a meaningful discordia cannot be calculated, all though generally the analyses are defining a trend similar to that in T01-40. Zr content is not correlated with the resetting of the rutile grains.

Figure 9: Calculated temperatures from Ti in zircon and Zr in rutile thermometry. Only analyses included in U–Pb age calculations were used in thermometry. Black line and grey bar indicate the calculated mean and uncertainty. **a)** Ti in zircon temperatures from T01-40. **b)** Ti in zircon temperatures from T06-09. **c)** Zr in rutile temperatures from T01-40 at 18 kbar. **d)** Zr in rutile temperatures from T06-09 at 18 kbar.

Figure 10: a) Mineral equilibria model calculated for T01-40 with water in excess, to model assemblages on the prograde path. Assemblages above the solidus were modelled with water set to 4.3 mol%. This was done as 4.3 mol% is the amount of water calculated to stabilise a water saturated solidus. Fields of interest are outlined in black bold line. The location of the omphacite-diopside solvus is marked in a thin grey dotted line. Colour of fields corresponds to variance in that field. **b)**

Same mineral equilibria model showing the range of compositions of plagioclase included in garnet in orange. The minimum and maximum Zr in rutile temperatures are plotted in black dashed line, with the individual uncertainties outlined in grey dashed lines. The grey shaded area represents the total range of Zr in rutile temperatures. Thick grey arrows indicate interpreted prograde *P*–*T* path. Abbreviations: Ab: Albite, Act: Actinolite, Coe: Coesite, Dio: Diopside, Ep: Epidote, G: Garnet, Gl: Glaucophane, Hb: Hornblende, Ilm: Ilmenite, L: Liquid (melt), Law: Lawsonite, Mt: Magnetite, O: Omphacite, Opx: Orthopyroxene, Pl: Plagioclase, Q: Quartz, Ru: Rutile, Ttn: Titanite.

Figure 11: a) Mineral equilibria model calculated for T01-40 with a set water content, used to model the peak to retrograde path. Fields of interest are outlined in black bold line. The location of the actinolite-hornblende solvus is marked in a thin grey dotted line. Colour of fields corresponds to variance in that field. **b)** Same mineral equilibria model with compositions and modal proportions of minerals of interest. The minimum and maximum Zr in rutile temperatures are plotted in black dashed line, with the individual uncertainties outlined in grey dashed lines. The grey shaded area represents the total range of Zr in rutile temperatures. Coloured thick lines indicate the modal proportion of labelled minerals, dashed coloured lines indicate the composition of labelled minerals. The transparent blue field covers the range of retrograde diopside $X_{(\mathrm{Fe})}$ compositions. Thick grey arrows indicate interpreted *P*–*T* path, the transparent grey arrow indicates the *P*–*T* path from Figure 10. Abbreviations: Ab: Albite, Act: Actinolite, Coe: Coesite, Dio: Diopside, Ep: Epidote, G: Garnet, Gl: Glaucophane, Hb: Hornblende, Ilm: Ilmenite, L: Liquid (melt), Law: Lawsonite, Mt: Magnetite, O: Omphacite, Opx: Orthopyroxene, Pl: Plagioclase, Q: Quartz, Ru: Rutile, Ttn: Titanite.

Figure 12: a) Mineral equilibria model calculated for T06-09 with a set water content, used to model the peak to retrograde path. Fields of interest are outlined in black bold line. Thin grey dotted lines mark the position of solvi. Colour of fields corresponds to variance in that field. **b)** Same mineral equilibria model with compositions and modal proportions of minerals of interest. The minimum and maximum Zr in rutile temperatures are plotted in black dashed line, with the individual uncertainties outlined in grey dashed lines. The grey shaded area represents the total range of Zr in

rutile temperatures. Coloured thick lines indicate the modal proportion of labelled minerals, dashed coloured lines indicate the composition of labelled minerals. The transparent blue field covers the range of retrograde diopside $X_{(Fe)}$ compositions. Thick grey arrows indicate interpreted *P*–*T* path. Abbreviations: Ab: Albite, Act: Actinolite, Coe: Coesite, Dio: Diopside, Ep: Epidote, G: Garnet, Gl: Glaucophane, Hb: Hornblende, Ilm: Ilmenite, L: Liquid (melt), Law: Lawsonite, Mt: Magnetite, O: Omphacite, Opx: Orthopyroxene, Pl: Plagioclase, Q: Quartz, Ru: Rutile, Ttn: Titanite.

Figure 13: Two possible tectonic scenarios for subduction and exhumation of the Usagaran retrogressed eclogites. **a-b)** Scenario involving east-dipping subduction of oceanic crust on the margin of the Tanzanian Craton under a continental ribbon previously rifted off the cratonic margin. After slab breakoff and docking of the ribbon, subduction polarity is reversed, placing the Isimani Suite in a back arc position. **c-d)** Scenario involving west-dipping subduction of oceanic crust under the Tanzanian Craton. After slab breakoff and docking of the rifted continental ribbon, subduction steps back, and the Isimani Suite is placed into a back arc position. **e-f)** Exhumation of the retrogressed eclogites in the back arc, and continued evolution of the Usagaran belt, including deposition and intrusion of the Konse Group and intrusion of arc-like granitoids and associated volcanics.

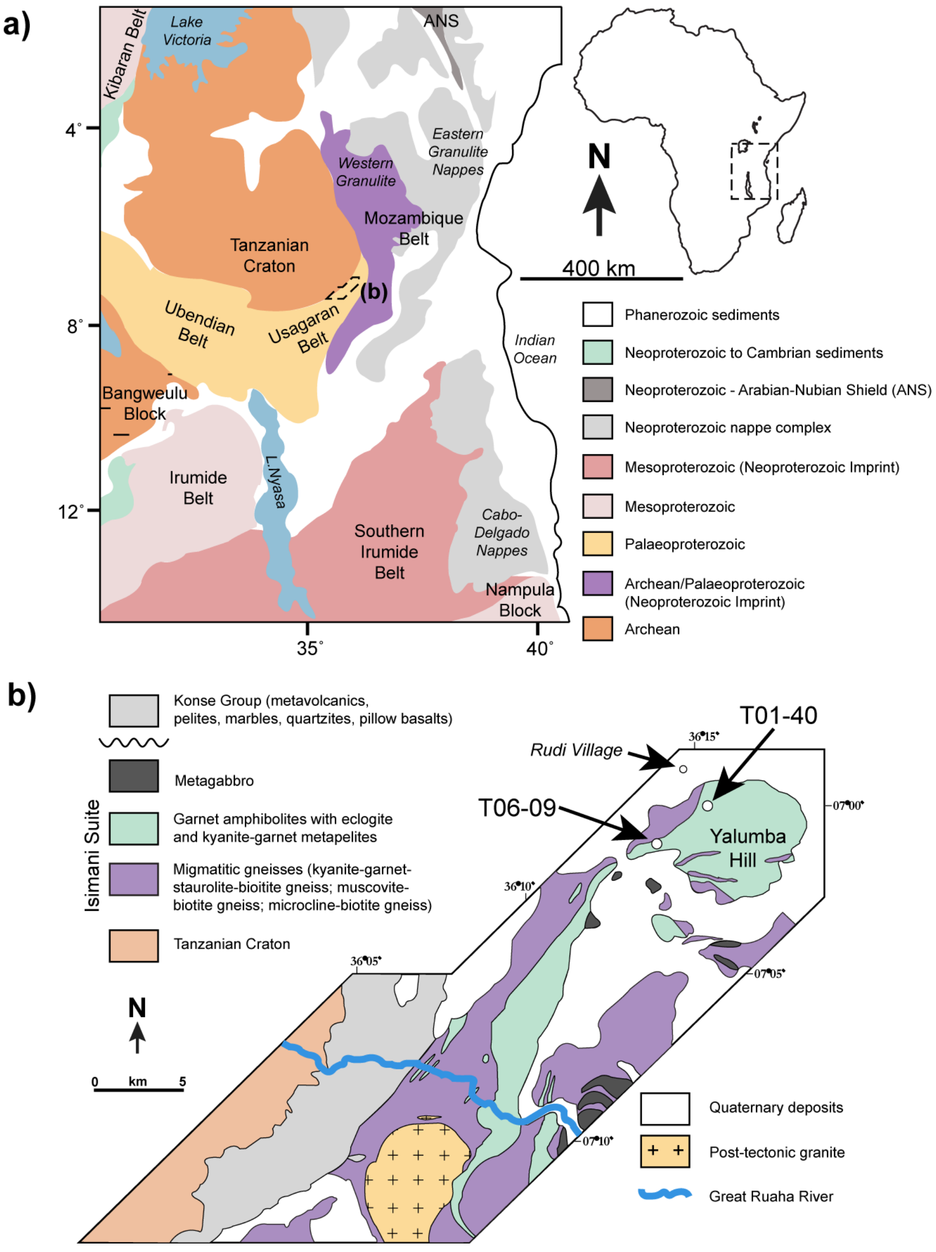
a)
Kibaran Belt
Lake Victoria
ANS
4°
8°
12°
35°
40°
Eastern Granulite Nappes
Western Granulite
Mozambique Belt
Tanzanian Craton
(b)
Ubendian Belt
Usagaran Belt
Bangweulu Block
Irumide Belt
L.Nyasa
Southern Irumide Belt
Cabo-Delgado Nappes
Nampula Block
Indian Ocean
N
400 km
Phanerozoic sediments
Neoproterozoic to Cambrian sediments
Neoproterozoic - Arabian-Nubian Shield (ANS)
Neoproterozoic nappe complex
Mesoproterozoic (Neoproterozoic Imprint)
Mesoproterozoic
Palaeoproterozoic
Archean/Palaeoproterozoic (Neoproterozoic Imprint)
Archean
b)
Konse Group (metavolcanics, pelites, marbles, quartzites, pillow basalts)
Metagabbro
Isimani Suite
Garnet amphibolites with eclogite and kyanite-garnet metapelites
Migmatitic gneisses (kyanite-garnet-staurolite-bioitite gneiss; muscovite-biotite gneiss; microcline-biotite gneiss)
Tanzanian Craton
N
0 km 5
T01-40
Rudi Village
T06-09
Yalumba Hill
36°15'
36°10'
36°05'
07°00'
07°05'
07°10'
Quaternary deposits
Post-tectonic granite
Great Ruaha River

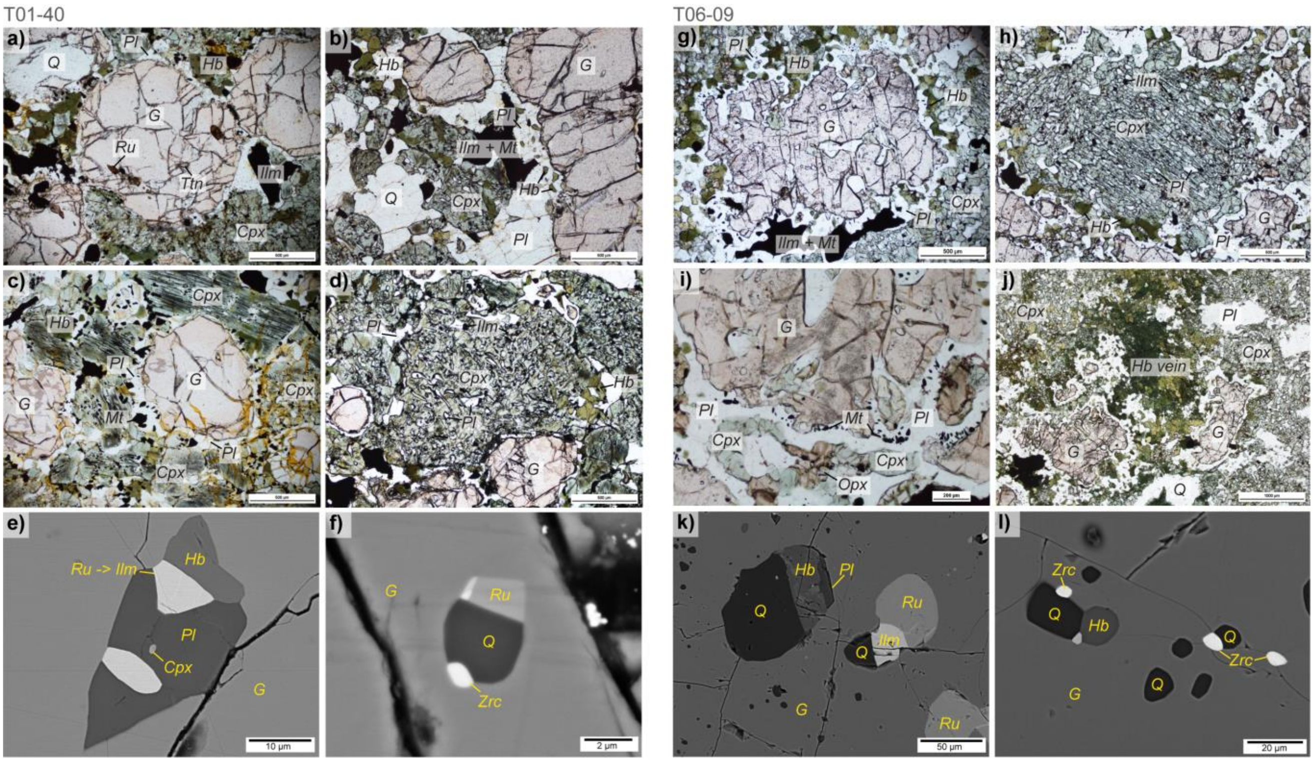
T01-40
T06-09
a)
Q
Pl
Hb
G
Ru
Ttn
Ilm
Cpx
b)
Hb
G
Pl
Ilm + Mt
Q
Cpx
Hb
Pl
c)
Cpx
Hb
Pl
G
G
Mt
Cpx
Pl
Cpx
d)
Pl
Ilm
Cpx
Hb
Pl
G
e)
Ru -> Ilm
Hb
Pl
Cpx
G
10 µm
f)
G
Ru
Q
Zrc
2 µm
g)
Pl
Hb
Hb
G
Cpx
Pl
Ilm + Mt
500 µm
h)
Ilm
Cpx
Pl
Hb
G
Pl
i)
G
Pl
Cpx
Mt
Pl
Cpx
Opx
j)
Cpx
Pl
Cpx
Hb vein
G
G
Q
k)
Hb
Pl
Q
Ru
Ilm
Q
G
Ru
50 µm
l)
Zrc
Q
Hb
Q
Zrc
G
Q
20 µm

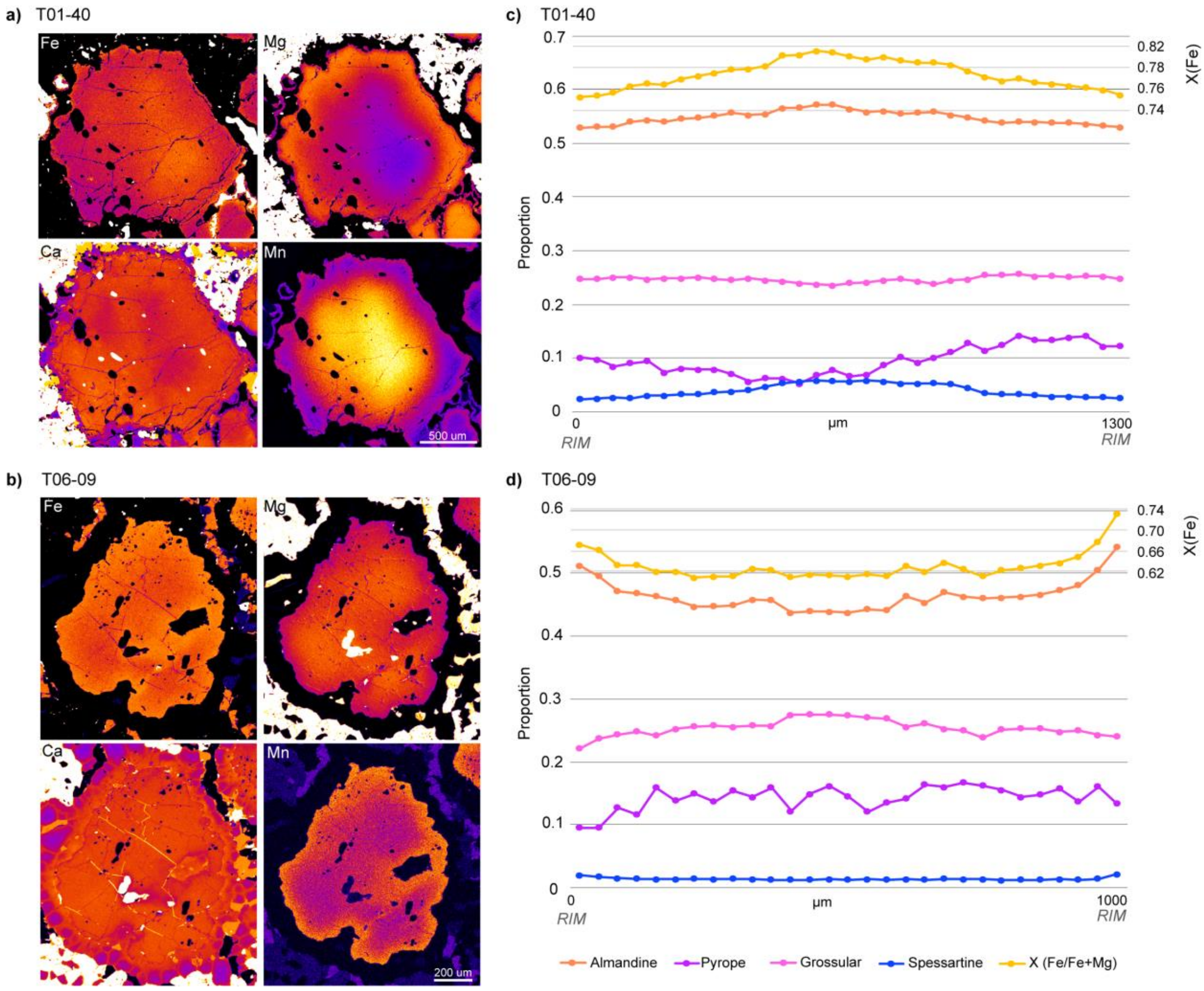

a) T01-40
Fe
Mg
Ca
Mn
500 um
b) T06-09
Fe
Mg
Ca
Mn
200 um
c) T01-40
Proportion
X(Fe)
µm
0
1300
RIM
RIM
d) T06-09
Proportion
X(Fe)
µm
0
1000
RIM
RIM
Almandine
Pyrope
Grossular
Spessartine
X (Fe/Fe+Mg)

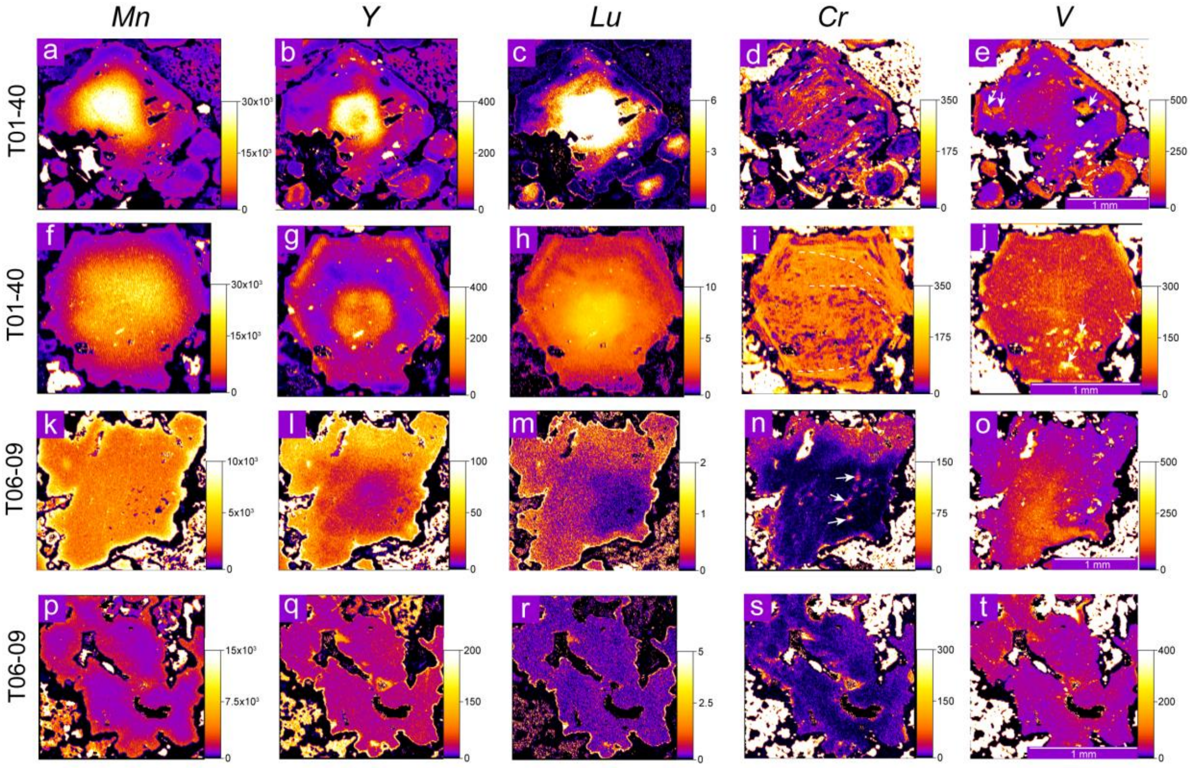
Mn
Y
Lu
Cr
V
T01-40
T01-40
T06-09
T06-09
1 mm

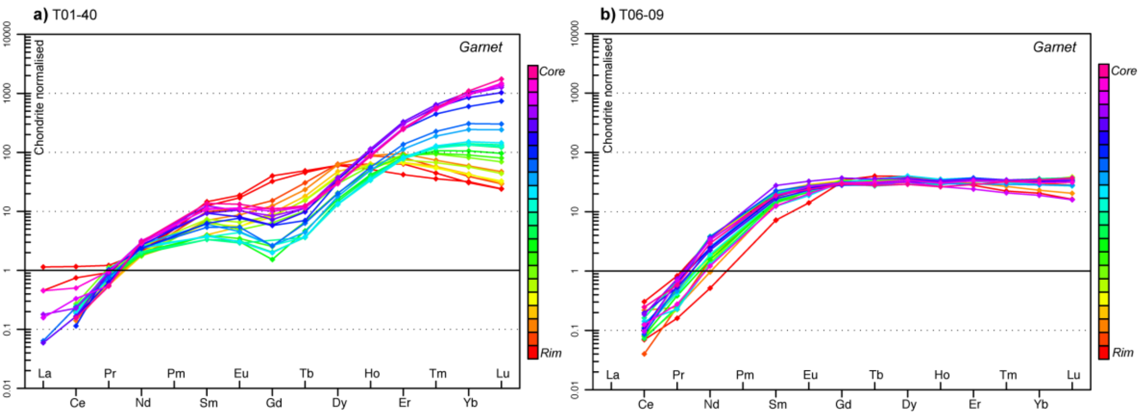
a) T01-40
b) T06-09
Garnet
Chondrite normalised
Core
Rim
La
Ce
Pr
Nd
Pm
Sm
Eu
Gd
Tb
Dy
Ho
Er
Tm
Yb
Lu

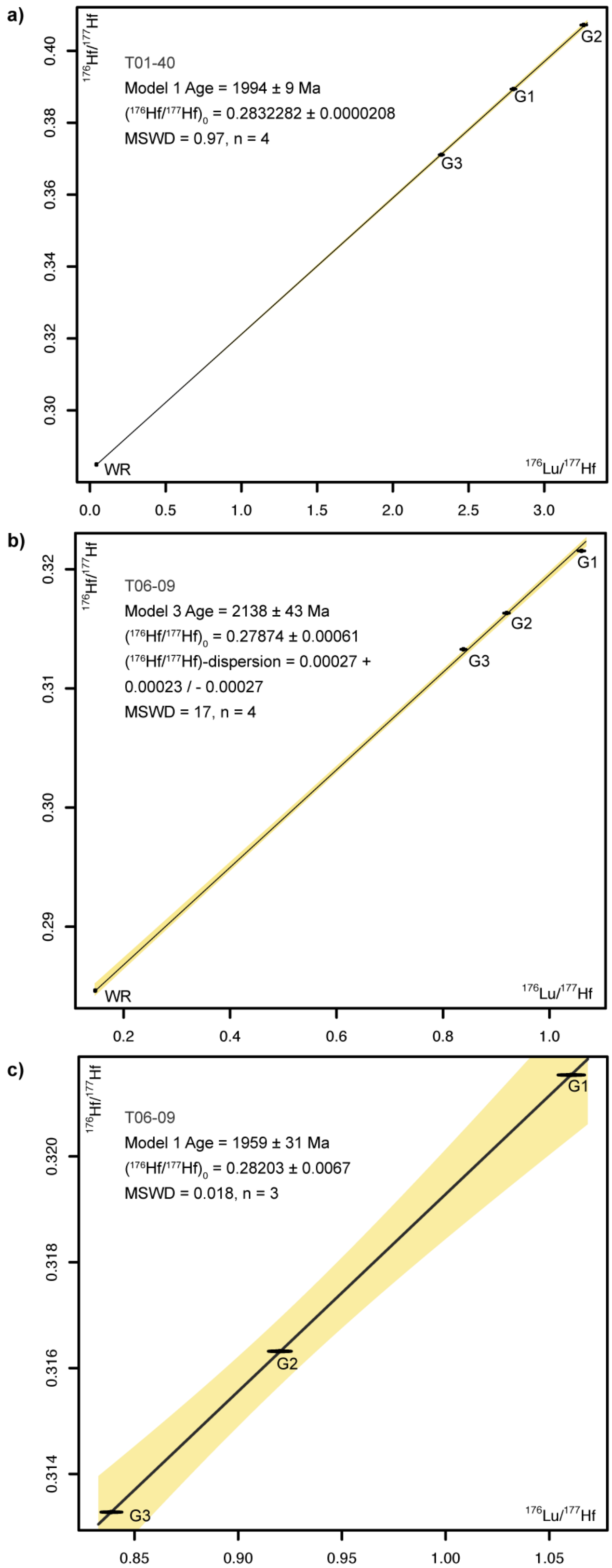
a)
T01-40
Model 1 Age = 1994 ± 9 Ma
(^{176}Hf/^{177}Hf)$_0$ = 0.2832282 ± 0.0000208
MSWD = 0.97, n = 4
G1
G2
G3
WR
^{176}Hf/^{177}Hf
^{176}Lu/^{177}Hf
b)
T06-09
Model 3 Age = 2138 ± 43 Ma
(^{176}Hf/^{177}Hf)$_0$ = 0.27874 ± 0.00061
(^{176}Hf/^{177}Hf)-dispersion = 0.00027 +
0.00023 / - 0.00027
MSWD = 17, n = 4
G1
G2
G3
WR
^{176}Hf/^{177}Hf
^{176}Lu/^{177}Hf
c)
T06-09
Model 1 Age = 1959 ± 31 Ma
(^{176}Hf/^{177}Hf)$_0$ = 0.28203 ± 0.0067
MSWD = 0.018, n = 3
G1
G2
G3
^{176}Hf/^{177}Hf
^{176}Lu/^{177}Hf

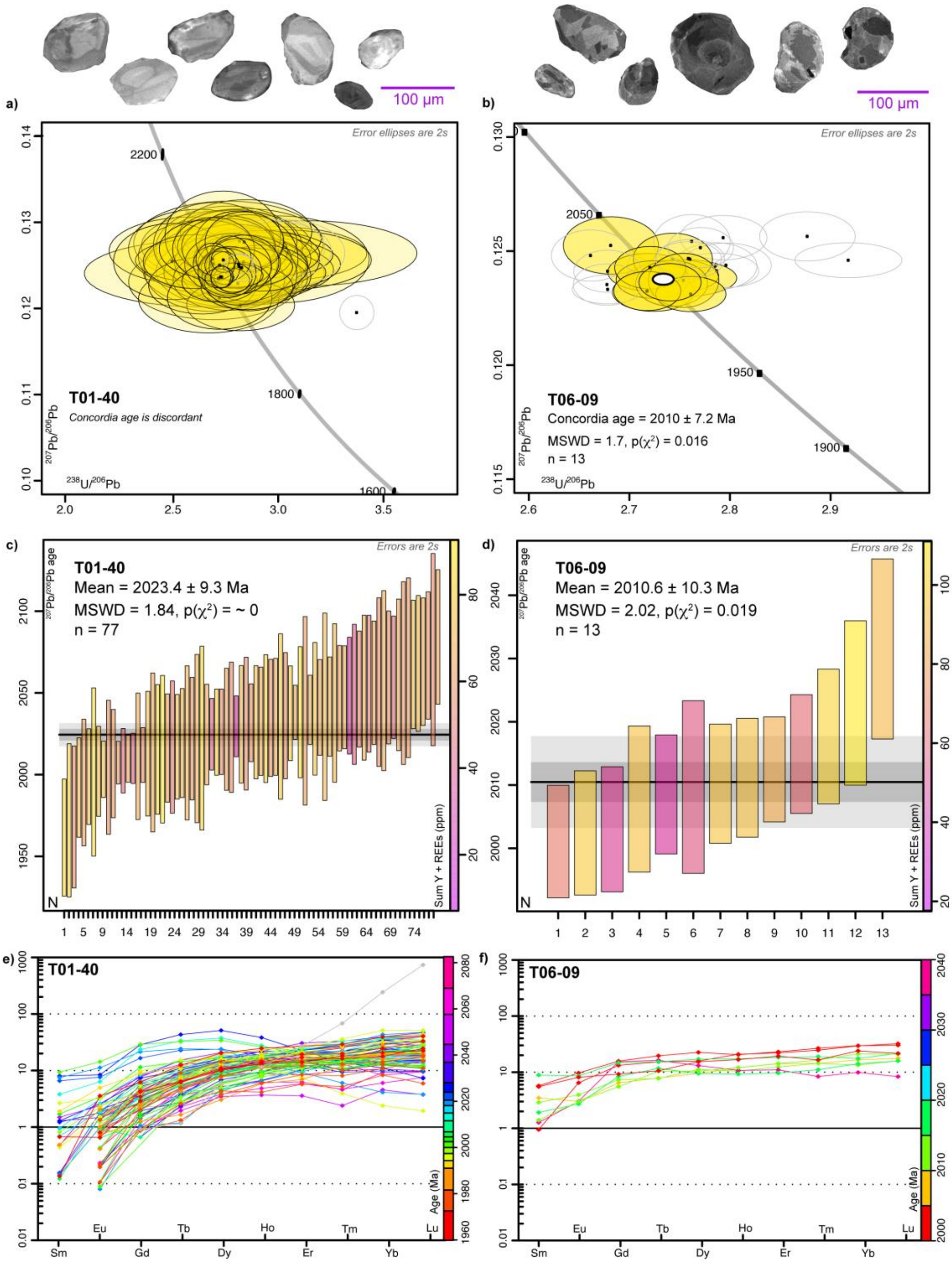

a)
100 μm
Error ellipses are 2s
2200
1800
1600
T01-40
Concordia age is discordant
$^{207}Pb/^{206}Pb$
$^{238}U/^{206}Pb$
b)
100 μm
Error ellipses are 2s
2050
1950
1900
T06-09
Concordia age = 2010 ± 7.2 Ma
MSWD = 1.7, p(χ²) = 0.016
n = 13
c)
Errors are 2s
T01-40
Mean = 2023.4 ± 9.3 Ma
MSWD = 1.84, p(χ²) = ~ 0
n = 77
$^{207}Pb/^{206}Pb$ age
Sum Y + REEs (ppm)
N
d)
Errors are 2s
T06-09
Mean = 2010.6 ± 10.3 Ma
MSWD = 2.02, p(χ²) = 0.019
n = 13
Sum Y + REEs (ppm)
N
e)
T01-40
Age (Ma)
Sm
Eu
Gd
Tb
Dy
Ho
Er
Tm
Yb
Lu
f)
T06-09
Age (Ma)

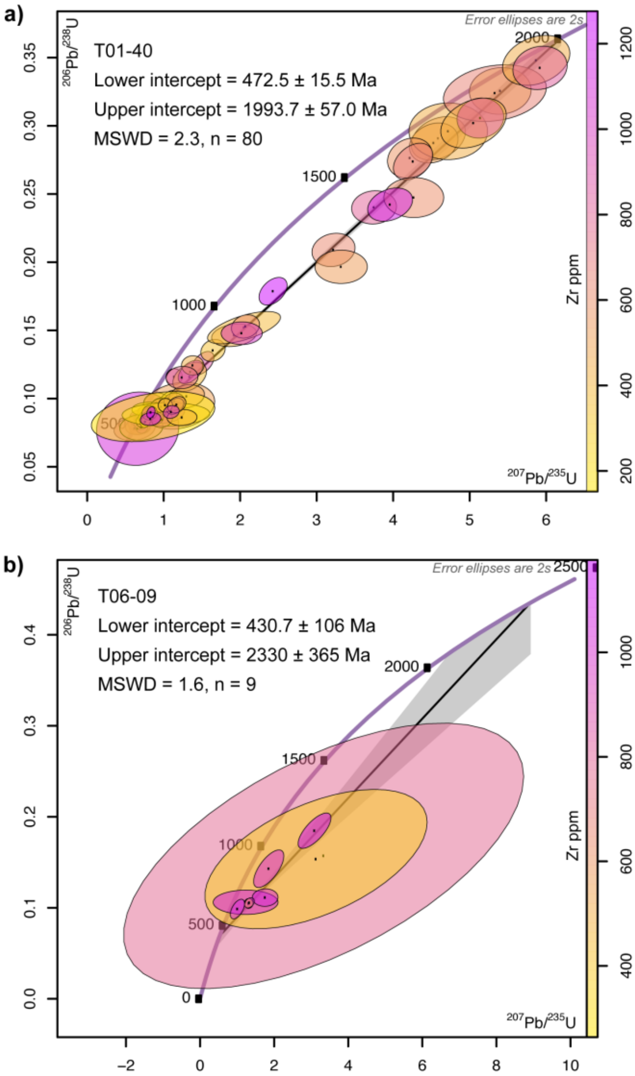
a)
Error ellipses are 2s
T01-40
Lower intercept = 472.5 ± 15.5 Ma
Upper intercept = 1993.7 ± 57.0 Ma
MSWD = 2.3, n = 80
500
1000
1500
2000
$^{206}Pb/^{238}U$
$^{207}Pb/^{235}U$
Zr ppm
b)
Error ellipses are 2s
T06-09
Lower intercept = 430.7 ± 106 Ma
Upper intercept = 2330 ± 365 Ma
MSWD = 1.6, n = 9
0
500
1000
1500
2000
2500
$^{206}Pb/^{238}U$
$^{207}Pb/^{235}U$
Zr ppm

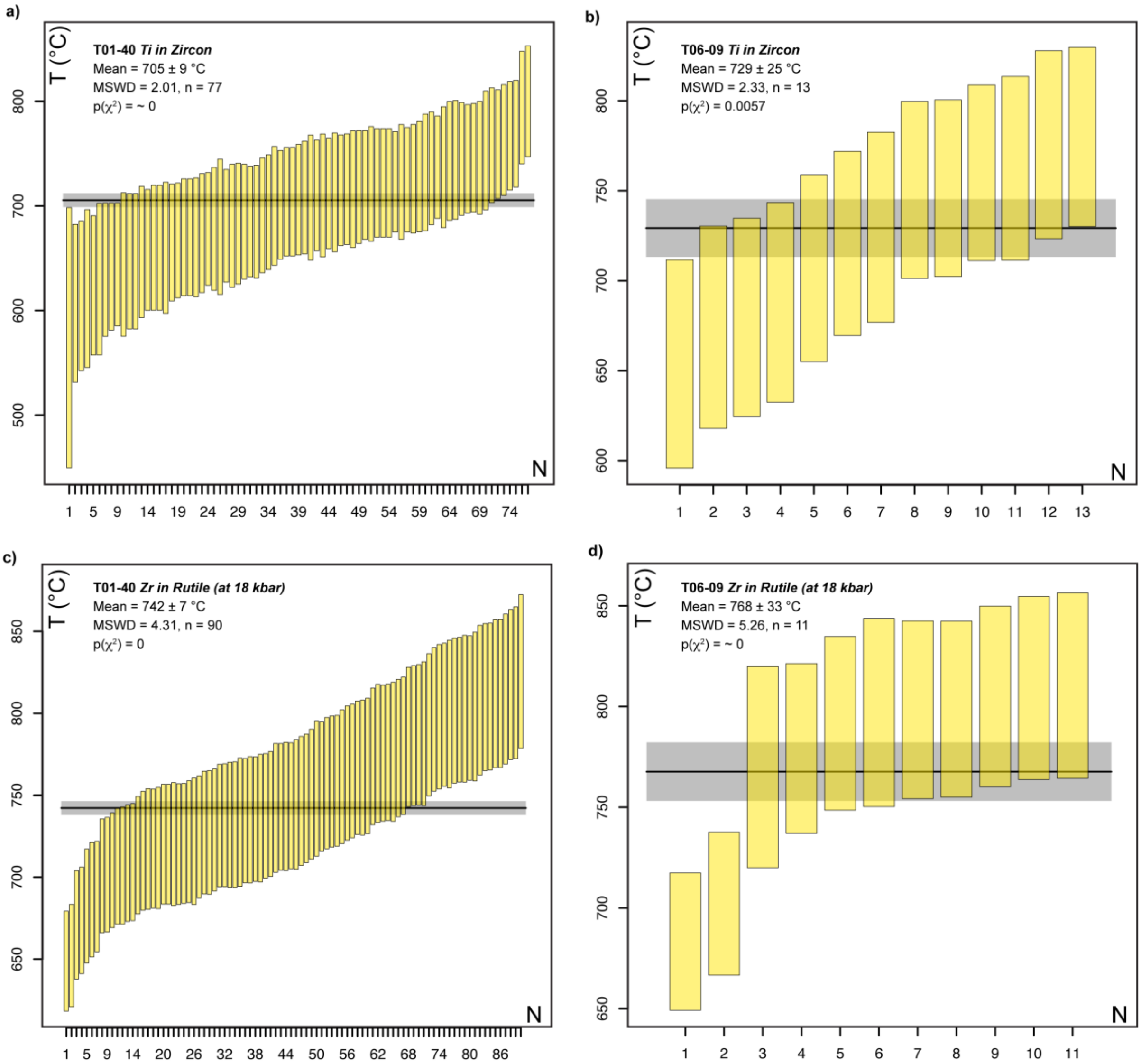
a)
T01-40 Ti in Zircon
Mean = 705 ± 9 °C
MSWD = 2.01, n = 77
p(χ²) = ~ 0
T (°C)
N
b)
T06-09 Ti in Zircon
Mean = 729 ± 25 °C
MSWD = 2.33, n = 13
p(χ²) = 0.0057
T (°C)
N
c)
T01-40 Zr in Rutile (at 18 kbar)
Mean = 742 ± 7 °C
MSWD = 4.31, n = 90
p(χ²) = 0
T (°C)
N
d)
T06-09 Zr in Rutile (at 18 kbar)
Mean = 768 ± 33 °C
MSWD = 5.26, n = 11
p(χ²) = ~ 0
T (°C)
N

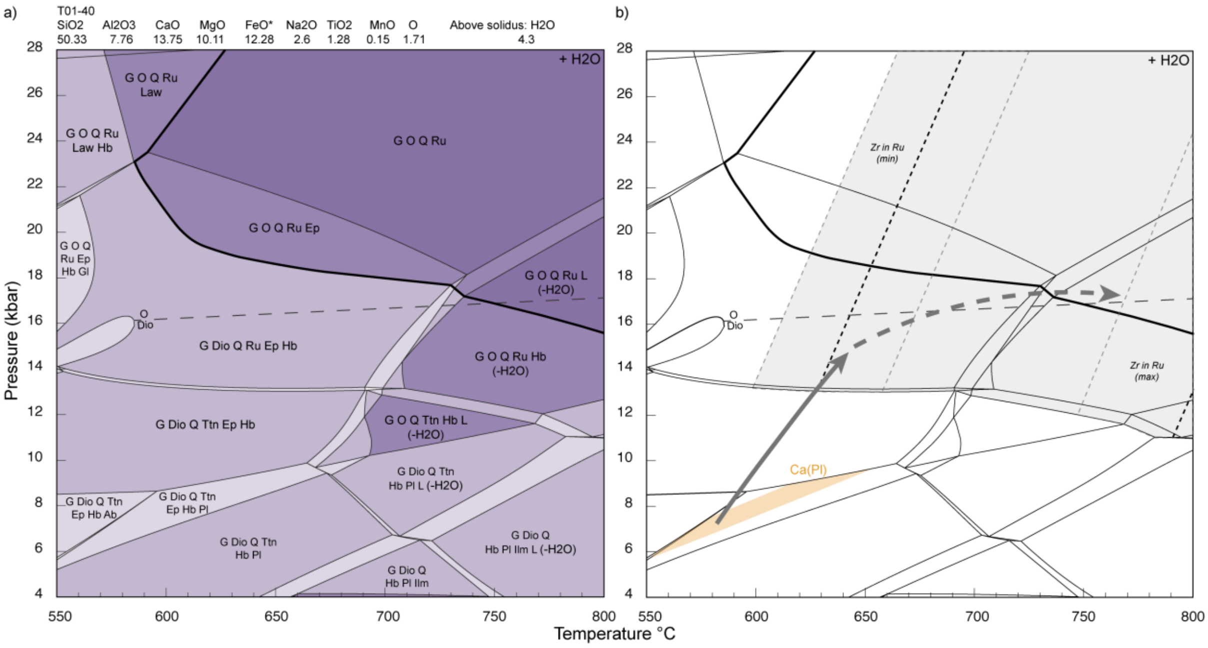

a)
T01-40
SiO2 Al2O3 CaO MgO FeO* Na2O TiO2 MnO O Above solidus: H2O
50.33 7.76 13.75 10.11 12.28 2.6 1.28 0.15 1.71 4.3
+ H2O
G O Q Ru Law
G O Q Ru Law Hb
G O Q Ru
G O Q Ru Ep
G O Q Ru Ep Hb Gl
G O Q Ru L (-H2O)
G Dio Q Ru Ep Hb
G O Q Ru Hb (-H2O)
G Dio Q Ttn Ep Hb
G O Q Ttn Hb L (-H2O)
G Dio Q Ttn Hb Pl L (-H2O)
G Dio Q Ttn Ep Hb Ab
G Dio Q Ttn Ep Hb Pl
G Dio Q Ttn Hb Pl
G Dio Q Hb Pl Ilm
G Dio Q Hb Pl Ilm L (-H2O)
O Dio
Pressure (kbar)
b)
Zr in Ru (min)
Zr in Ru (max)
Ca(Pl)
Temperature °C

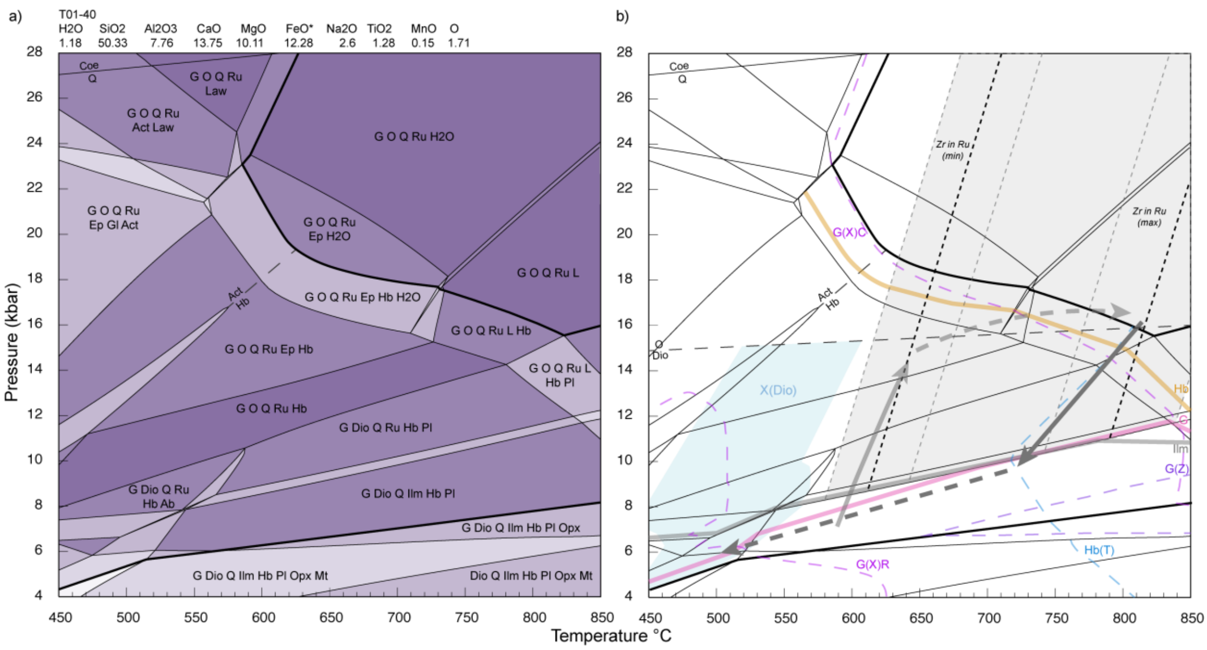

a)
T01-40
H2O SiO2 Al2O3 CaO MgO FeO* Na2O TiO2 MnO O
1.18 50.33 7.76 13.75 10.11 12.28 2.6 1.28 0.15 1.71
Coe Q
G O Q Ru Law
G O Q Ru Act Law
G O Q Ru H2O
G O Q Ru Ep Gl Act
G O Q Ru Ep H2O
G O Q Ru L
Act Hb
G O Q Ru Ep Hb H2O
G O Q Ru L Hb
G O Q Ru Ep Hb
G O Q Ru L Hb Pl
G O Q Ru Hb
G Dio Q Ru Hb Pl
G Dio Q Ru Hb Ab
G Dio Q Ilm Hb Pl
G Dio Q Ilm Hb Pl Opx
G Dio Q Ilm Hb Pl Opx Mt
Dio Q Ilm Hb Pl Opx Mt
Pressure (kbar)
b)
Zr in Ru (min)
Zr in Ru (max)
G(X)C
X(Dio)
O Dio
Hb
C
Ilm
G(Z)
G(X)R
Hb(T)
Temperature °C

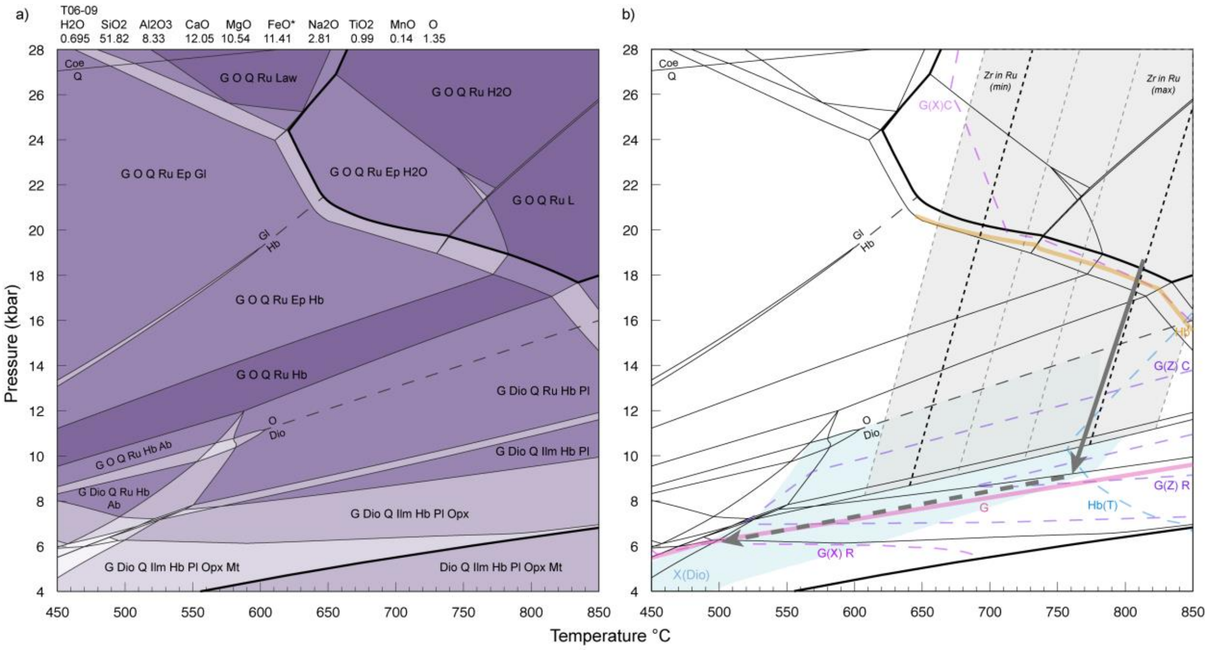
a)
T06-09
H2O SiO2 Al2O3 CaO MgO FeO* Na2O TiO2 MnO O
0.695 51.82 8.33 12.05 10.54 11.41 2.81 0.99 0.14 1.35
Coe
Q
G O Q Ru Law
G O Q Ru H2O
G O Q Ru Ep Gl
G O Q Ru Ep H2O
G O Q Ru L
Gl
Hb
G O Q Ru Ep Hb
G O Q Ru Hb
G Dio Q Ru Hb Pl
O
Dio
G O Q Ru Hb Ab
G Dio Q Ilm Hb Pl
G Dio Q Ru Hb Ab
G Dio Q Ilm Hb Pl Opx
G Dio Q Ilm Hb Pl Opx Mt
Dio Q Ilm Hb Pl Opx Mt
Pressure (kbar)
b)
Zr in Ru (min)
Zr in Ru (max)
G(X)C
G(Z) C
G(Z) R
Hb(T)
G
G(X) R
X(Dio)
Temperature °C

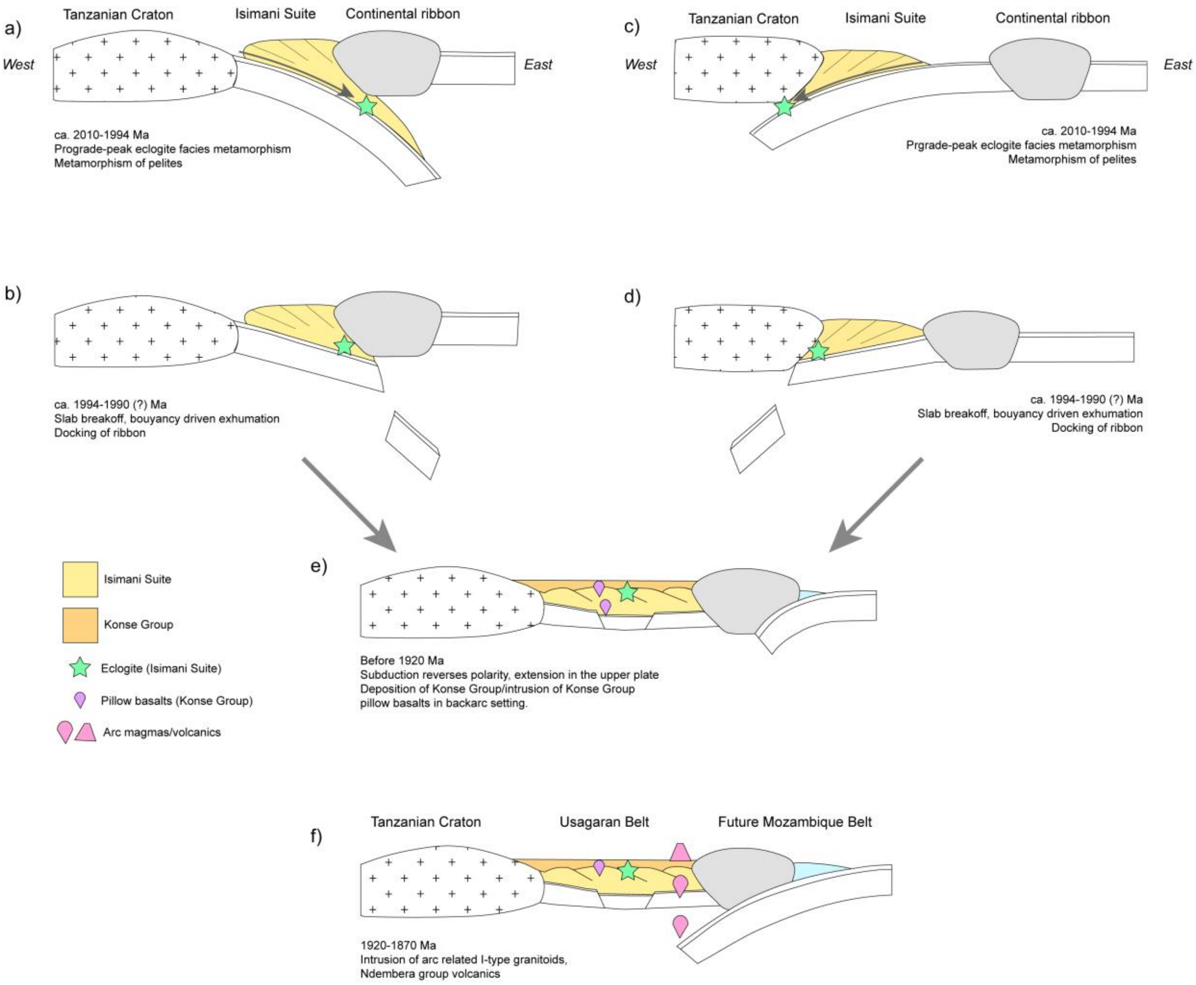
a)
Tanzanian Craton
Isimani Suite
Continental ribbon
West
East
ca. 2010-1994 Ma
Prograde-peak eclogite facies metamorphism
Metamorphism of pelites
c)
Tanzanian Craton
Isimani Suite
Continental ribbon
West
East
ca. 2010-1994 Ma
Prgrade-peak eclogite facies metamorphism
Metamorphism of pelites
b)
ca. 1994-1990 (?) Ma
Slab breakoff, bouyancy driven exhumation
Docking of ribbon
d)
ca. 1994-1990 (?) Ma
Slab breakoff, bouyancy driven exhumation
Docking of ribbon
Isimani Suite
Konse Group
Eclogite (Isimani Suite)
Pillow basalts (Konse Group)
Arc magmas/volcanics
e)
Before 1920 Ma
Subduction reverses polarity, extension in the upper plate
Deposition of Konse Group/intrusion of Konse Group
pillow basalts in backarc setting.
f)
Tanzanian Craton
Usagaran Belt
Future Mozambique Belt
1920-1870 Ma
Intrusion of arc related I-type granitoids,
Ndembera group volcanics